PASJ: Publ. Astron. Soc. Japan **59**, S53–S76, 2007 January 25

In-Orbit Performance of the Hard X-Ray Detector on Board Suzaku

Motohide KOKUBUN,[1] Kazuo MAKISHIMA,[1,2] Tadayuki TAKAHASHI,[3,1] Toshio MURAKAMI,[4] Makoto TASHIRO,[5] Yasushi FUKAZAWA,[6] Tuneyoshi KAMAE,[9] Greg M. MADEJSKI [9] Kazuhiro NAKAZAWA,[3] Kazutaka YAMAOKA,[7] Yukikatsu TERADA,[2] Daisuke YONETOKU,[4] Shin WATANABE,[3] Toru TAMAGAWA,[2] Tsunefumi MIZUNO,[6] Aya KUBOTA,[2] Naoki ISOBE,[2] Isao TAKAHASHI,[1] Goro SATO,[3] Hiromitsu TAKAHASHI,[6] Soojing HONG,[8] Madoka KAWAHARADA,[1] Naomi KAWANO,[6] Takefumi MITANI,[3] Mio MURASHIMA,[1] Masaya SUZUKI,[5] Keiichi ABE,[5] Ryouhei MIYAWAKI,[1] Masanori OHNO,[6] Takaaki TANAKA,[3,1] Takayuki YANAGIDA,[1] Takeshi ITOH,[1] Kousuke OHNUKI,[3,1] Ken-ichi TAMURA,[3,1] Yasuhiko ENDO,[5] Shinya HIRAKURI,[1] Tatsuro HIRUTA,[3] Takao KITAGUCHI,[1] Tetsuichi KISHISHITA,[3,1] Satoshi SUGITA,[7] Takuya TAKAHASHI,[6] Shin'ichiro TAKEDA,[3,1] Teruaki ENOTO,[1] Ayumi HIRASAWA,[6] Jun'ichiro KATSUTA,[3,1] Satoshi MATSUMURA,[5] Kaori ONDA,[5] Mitsuhiro SATO,[1] Masayoshi USHIO,[3,1] Shin-nosuke ISHIKAWA,[3,1] Koichi MURASE,[5] Hirokazu ODAKA,[3,1] Masanobu SUZUKI,[5] Yuichi YAJI,[5] Shinya YAMADA,[1] Tomonori YAMASAKI,[6] Takayuki YUASA,[1] and the HXD team

[1]*Department of Physics, The University of Tokyo, 7-3-1 Hongo, Bunkyo-ku, Tokyo 113-0033*
kokubun@phys.s.u-tokyo.ac.jp
[2]*Cosmic Radiation Laboratory, The Institute of Physical and Chemical Research (RIKEN), 2-1 Hirosawa, Wako, Saitama 351-0198*
[3]*Department of High Energy Astrophysics, Institute of Space and Astronomical Science (ISAS), Japan Aerospace Exploration Agency (JAXA), 3-1-1 Yoshinodai, Sagamihara, Kanagawa 229-8510*
[4]*Department of Physics, Kanazawa University, Kakuma, Kanazawa, Ishikawa 920-1192*
[5]*Department of Physics, Saitama University, 255 Shimo-Okubo, Sakura-ku, Saitama 338-8570*
[6]*Department of Physical Science, Hiroshima University, 1-3-1 Kagamiyama, Higashi-Hiroshima, Hiroshima 739-8526*
[7]*Department of Physics and Mathematics, Aoyama-Gakuin University, 5-10-1 Fuchinobe, Sagamihara, Kanagawa 229-8558*
[8]*College of Science and Technology, Nihon University, 7-24-1 Narashinodai, Funabashi, Chiba 274-8501*
[9]*Stanford Linear Accelerator Center, 2575 Sand Hill Road, Menlo Park, CA 94025, USA*

(Received 2006 September 6; accepted 2006 October 15)

Abstract

The in-orbit performance and calibration of the Hard X-ray Detector (HXD) on board the X-ray astronomy satellite Suzaku are described. Its basic performances, including a wide energy bandpass of 10–600 keV, energy resolutions of ~ 4 keV (FWHM) at 40 keV and $\sim 11\%$ at 511 keV, and a high background rejection efficiency, have been confirmed by extensive in-orbit calibrations. The long-term gains of PIN-Si diodes have been stable within 1% for half a year, and those of scintillators have decreased by 5–20%. The residual non-X-ray background of the HXD is the lowest among past non-imaging hard X-ray instruments in energy ranges of 15–70 and 150–500 keV. We provide accurate calibrations of energy responses, angular responses, timing accuracy of the HXD, and relative normalizations to the X-ray CCD cameras using multiple observations of the Crab Nebula.

Key words: instrumentation: detectors — X-rays: general — X-rays: individual (Crab Nebula)

1. Introduction

The fifth Japanese X-ray satellite, Suzaku, was launched on 2005 July 10 into a low Earth orbit of ~ 570 km altitude and 32° inclination (Mitsuda et al. 2007). The satellite carries four X-ray CCD cameras (X-ray Imaging Spectrometer — XIS, Koyama et al. 2007), which are placed at the focal points of the four X-ray telescopes (XRT, Serlemitsos et al. 2007) and cover the soft energy range of 0.2–12 keV. The satellite also carries a non-imaging hard X-ray instrument, the Hard X-ray Detector (HXD), which is the subject of the present paper. The detailed design of the experiment and basic performances in the pre-launch calibration are described by Takahashi et al. (2007, hereafter Paper I), followed by brief descriptions of the initial in-orbit performance by Fukazawa et al. (2006) and Kitaguchi et al. (2006).

The HXD consists of three parts contained in separate chassis: the sensor (hereafter HXD-S), the analog electronics (HXD-AE), and the digital electronics (HXD-DE). The HXD achieves an extremely low detector background through a highly ingenious structure of HXD-S, a compound-eye configuration of 4×4 well-type phoswich units ("Well units") surrounded by 20 thick active shields ("Anti units"). In addition to signals from all of 36 units, those from 64 PIN-Si diodes inside the well-type phoswiches are also fed into the parallel readout system in HXD-AE, and the hard-wired anti-coincidence system drastically reduces the detector background by using the hit-pattern signal from active shields. Further intelligent event screenings are realized by the onboard software in HXD-DE (Paper I).

Extensive in-orbit calibrations for all of the hundred signals are crucial to confirm that the instrument survived the launch, to optimize the hardware/software settings and the daily operation scheme of the HXD, and to verify the detector

Table 1. Run-up operation procedures of the HXD.

Date	Operation
July 11–13	HXD-S temperature 20 °C → −15 °C
July 22	HXD on, HXD-DE on, CPU run, observation mode
	HXD-S temperature −15 °C → −20 °C
July 25	WPU0-3 on, TPU0-3 on, HXD-AE initial parameter load
July 27	HV-W0-3, HV-T0-3, HV-P0-3 on
July 27–August 4	HV operation, AE/DE parameter tuning
August 8–15	HV reduction
August 15–18	HV operation, AE/DE parameter tuning
August 19	First-light (Cen A)

performance in orbit. We summarize the in-orbit operations in section 2. The in-orbit performances of PIN-Si diodes (hereafter PIN) and the gadolinium silicate scintillators (Gd_2SiO_5:Ce, hereafter GSO) are described in sections 3 and 4, respectively. The spectral and temporal properties of the residual background are explained in section 5. In section 6, we address other miscellaneous calibration issues, including the angular response, dead-time estimation, and timing accuracy.

2. Initial Operation of the HXD

On 2005 July 22, about two weeks after the launch, a run-up operation of the electronic system of HXD started. It took a few days to turn on the low-voltage part of the experiment, and upload initial settings of the onboard hardware and software. After that, an extended period of high-voltage turn-on followed over a one-week, in which parameter tuning of the electronics was also performed. These operations are summarized in table 1.

2.1. Temperature Control of HXD

The heat generated from electrical power consumption in HXD-S is transported through two sets of heat-pipes, which are thermally connected to "cold plate" beneath HXD-S, and then released from two radiators on the spacecraft side panels numbers 6 and 8 (Mitsuda et al. 2007). The cooling is compensated by two pairs of heaters, which are also attached to the cold plate. Thus, the temperature of HXD-S is designed to be controlled in the orbit within −20 °C ± 5 °C (Paper I), which is the optimum for low thermal noise in PIN and high light yields in scintillators.

Since a large temperature gradient within HXD-S would cause excess thermal strain to the scintillators, the HXD-S temperature should be changed gradually, by no more than a limit of 5° per hour. On the day following the launch, solar array panels were opened and the temperatures of the instruments inside the spacecraft started decreasing rapidly. The temperature of the cold plate of HXD-S was thus controlled to drop from 20 °C to −15 °C with steps of 5° or 2.°5, during contact passes of the succeeding three days. It was then further lowered to the nominal operation temperature, −20 °C, after turn-on of HXD-DE.

In the very early phase of this temperature-control operation, it was found that one of the two heat-pipes, connected to the radiator on side panel 6, was not functional, implying that the available heat transport capability became half of the designed value. As a result, the actual temperature of HXD-S remained around −16 °C, even though the control temperature was set to −20 °C. Furthermore, the temperature could not be "controlled" to sufficiently low values, and hence it fluctuated due to attitude changes of the satellite, which affected solar heat in-flows to the spacecraft. To measure long-term gain variations of photo-multiplier tubes (PMTs) free of temperature-dependent gain changes, the control temperature was changed to −14.5 °C on 2005 November 16 until 2006 March 22. Although it was feared that the higher HXD-S temperature would enhance the thermal noise of the PIN diodes, the effect was confirmed to appear only at an energy range lower than 10–12 keV (subsection 3.2), as long as the temperature is below −11 °C. The resultant temperature light curve of HXD-S, measured at the cold plates, is shown in figure 1.

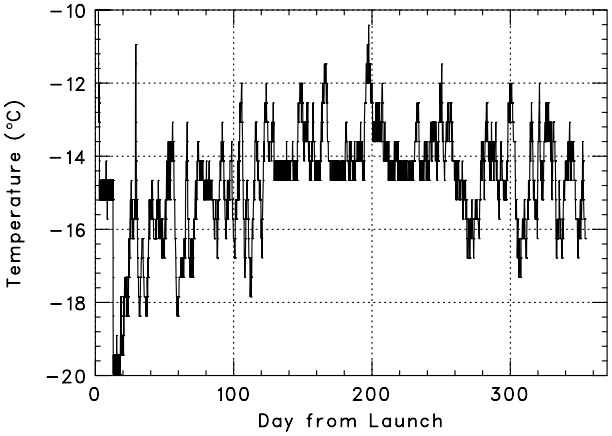

Fig. 1. Temperature history of HXD-S measured at the cold plate for about one year from the launch. The control temperature was kept at −14.5 °C from 129 to 255 days after the launch.

2.2. High-Voltage Operations

HXD-S uses four high-voltage supply units for PIN diodes (PIN-HV), which can provide up to 600 V, and eight units for PMTs (PMT-HV) up to 1250 V. One PMT-HV drives four PMTs that share the same electronics module (WPU or TPU, Paper I), while one PIN-HV supplies bias voltages for

Table 2. Nominal high voltages.

	HV unit #			
	0	1	2	3
PIN	489	489	490	490
PMT (Well)	850	872	875	902
PMT (Anti)	816	860	878	874

16 diodes. When increasing the PIN-HV output, a step increment of less than 100 V is used so as not to destroy FETs inside the charge-sensitive preamplifiers.

High-voltage run-up operation started after a 17-day waiting period to let the spacecraft fully outgas, and to prevent the high voltages from discharging. The PIN-HVs were first operated at low voltages (50 V) for short intervals (~ 10 min) when the satellite kept in contact with the tracking station. Even with this low bias voltage, large pulse-height events, caused by cosmic-ray particles penetrating the detector, were observed at a rate of $\sim 10\,\mathrm{ct\,s^{-1}}$ (summed over the 4 PIN diodes in the same phoswich unit). Using such particle events, all the 64 diodes were confirmed to have survived the severe launch vibration. Then, over about a one-week period, the operation voltage and its duty cycle were gradually increased to the nominal values of ~ 500 V and 100%.

After confirmation of the normal functioning of the PIN diodes and PIN-HVs, the output voltage from the PMT-HVs was also increased to 500 V. At this stage, all PMT units were confirmed to be properly functioning by the use of cosmic-ray events. In addition, anti-coincidence particle reduction with the hit-pattern signals was also confirmed to be working as designed. The operation voltages and the duty cycle were gradually increased in the same manner as the PIN-HV, up to individual nominal voltages, which were determined from pre-launch gain measurements. Table 2 summarizes the achieved final operation voltages for all high-voltage units, which remained unchanged throughout the performance verification phase.

The outputs from PMT-HVs are all reduced to zero by programmed commands during the South Atlantic Anomaly (SAA) passages, in which a huge number of charged particles hit the detector. This manual operation is backed up with an automatic control by a radiation belt monitor (RBM) function, based on the counting rates of four corner shield units (Paper I; Yamaoka et al. 2006). The RBM flag was sometimes triggered by intense solar flares in the early phase, and it was confirmed that the reduction sequence works properly. While a nominal counting rate of one corner unit is $\sim 1000\,\mathrm{ct\,s^{-1}}$, it is expected to reach a few $10\,\mathrm{kct\,s^{-1}}$ when the PMT-HVs are accidentally not reduced during SAA passage, and the actual counting rate in the solar-side two units recorded more than $25\,\mathrm{kct\,s^{-1}}$ in an X2.0 class solar flare. Therefore, the threshold rates of the RBM function were finalized as $100\,\mathrm{kct\,s^{-1}}$ for the solar-side units (T00, T10) and $10\,\mathrm{kct\,s^{-1}}$ for the others (T20, T30).

2.3. *Electronics Setup*

HXD-AE has various adjustable parameters, which can be changed by commands for individual detector units (Paper I). On July 25, HXD-AE was tentatively loaded with a nominal parameter table, which was determined based on a ground calibration. After high-voltage operation was mostly completed, each parameter was re-optimized according to the in-orbit data. For both PIN and GSO, the hardware event selection with lower and upper discriminators (LD and UD) and pulse-shape discrimination (PSD) was set to be as loose as possible, provided that the data transfer rate from HXD-AE to HXD-DE stays within the hardware limit of 128 kbps (~ 1000 events $\mathrm{s^{-1}}$) per WPU (Paper I). The achieved final parameters are summarized in table 3.

In the case of PIN, the pulse heights from all the 64 diodes are adjustable with a common gain for every four gain-amplifiers, while trigger signals are produced at comparators, which have also a common threshold voltage in each WPU. Then, the triggers produce corresponding event records with a sampling resolution of 8-bits (256 bins). The gains and LD levels have been kept almost the same as the nominal ones in all of the PIN diodes, because their performance did not

Table 3. Nominal setup of HXD-AE.

	Setting	Energy*	Common units†
PIN			
Gain	$\times 5.0$		4 PIN
Analog LD	68–85 mV	6–8 keV	16 PIN
PMT			
Slow gain	$\times 2.0$–2.4		individual
Fast gain	$\times 2.2$–2.5		individual
PSD level	300–400 mV	30–40 keV	4 well
Anode LD level	30–40 mV	25–30 keV	individual
SLD level	125–133 mV	15–20 keV	individual
UD level	2.06 V	800–900 keV	4 well
UD veto width	40 μs		4 well
Hit-pattern width	5.6 μs		4 well

* Rough conversion into the energy.
† Number of PIN diodes or well units, which are commonly applied with the same parameter.

change significantly after the launch. The final settings allow a dynamic range of 8–90 keV, which completely satisfies the design goals, and the digitization of 256 channel pulse-height spectrum, $\sim$0.4 keV per channel, are fine enough for the typical energy resolution of the PIN diodes ($\sim$ 4 keV).

The counting rates of the LD and UD from every four PIN diodes (PIN-LD and PIN-UD) in a same well unit, recorded by scalers in HXD-AE, are edited every telemetry period (nominally 2 or 4 s) into the house keeping (HK) data, and utilized to monitor the raw trigger rates before the onboard event reduction. While the PIN-LD rate from most of 16 units stays within 10–50 ct s^{-1} in orbit, some units sometimes exhibit exceptionally high counting rates of $> 100\,\mathrm{ct\,s^{-1}}$, especially during the daytime of the satellite. This is thought to be caused by electrical interference from a large surplus current of the solar paddle, which is dissipated at shunt resistors on the side-panel.

Although the PIN-Si diodes employed in the HXD have an unprecedented thickness of 2 mm (Paper I), they have negligible ($\leq 1\%$) cross-sections for hard X-ray photons with energies higher than the UD level ($\sim$ 90 keV); therefore, the counting rate of the PIN-UD can be regarded as the number of cosmic-ray charged particles penetrating the device. A typical in-orbit rate of the PIN-UD is $\sim 10\,\mathrm{ct\,s^{-1}}$ per well unit, corresponding to $\sim$ 1 particle $s^{-1}\,cm^{-2}$. As mentioned later (subsection 5.1), this method can also be applied to estimate the particle flux during the SAA, since the high-voltages for the PIN diodes are always kept on.

In contrast to the case of the PIN diodes, various in-orbit fine tunings were necessary for GSO, mainly because PMT gains can generally, and did actually, change by up to $\sim$ 10% due to the launch vibration. The relative gains of the 16 well units were first adjusted by trimming gain-amplifiers for the "slow" shaping signals in HXD-AE, using the intrinsic natural radioactive isotope (^{152}Gd, Paper I). The "fast" gains were also trimmed for the GSO events to have the same pulse heights as their "slow" pulse heights. As a result, the slope of the GSO branch on the 2-dimensional fast–slow diagram became close to diagonal, and hence the hardware PSD cut can utilize the same conditions as those optimized on the ground.

The LD levels of the anode trigger (anode LD) were set for individual units at around 30 keV, while the UD levels were set at $\sim$ 900 keV, shared by four units. Another lower threshold, called "slow LD" (SLD), which is applied to the slow shaped signal to generate hit-pattern flags, was kept at the pre-launch value in all units. The SLD level corresponds to an energy deposit of $\sim$ 20 keV if it occurs in GSO, $\sim$ 50 keV if in the bottom block of the BGO shield, and $\sim$ 100 keV if in the Well-shaped BGO top part. With these settings, typical counting rates of LD, UD, and SLD from one unit are 700–1000 $\mathrm{ct\,s^{-1}}$, 50–100 ct s^{-1}, and 1000–1500 ct s^{-1}, respectively. Although each anode trigger initiates a data-acquisition sequence, most of them are immediately rejected before the analog-to-digital conversion stage when the hard-wired PSD function is enabled, and the rate of events acquired as digitized data packets is successfully reduced to be less than $\sim 100\,\mathrm{ct\,s^{-1}}$.

The widths of the hit-pattern signals from both the Well and Anti units are also adjustable from 4.2 to 5.6 μs by commands (Paper I). A longer width usually yields a higher reduction efficiency of the anti-coincidence, at the sacrifice of an increase of the accidental coincidence. Two different widths of 4.6 and 5.6 μs were tested during an observation of a blank-sky field to investigate the optimum in the orbit. Since the longer one yielded a significantly ($\sim$ 20%) lower background of the PIN diodes with only a small increase ($\sim$ 1%) of the accidental coincidence, the latter was employed. The widths of trigger generation vetoing, which suppresses false triggers after large signals above the UD level, were fixed to be the same as that optimized on the ground (40 μs).

2.4. *Onboard Software Setup*

Even after a hard-wired PSD cut, the total event rate summed over the four WPU modules typically reached a few $\mathrm{kct\,s^{-1}}$, significantly higher than the nominal telemetry limit ($\sim 300\,\mathrm{ct\,s^{-1}}$), mainly due to electrical interferences and insufficient temperature control after the launch. However, the onboard software in HXD-DE had been designed to be flexible with its various event-selection functions, and hence further event reductions can be achieved. The onboard software can judge events based on the PIN or GSO pulse heights, as well as subsidiary information, such as the trigger pattern, hit-pattern, and quality flags (Paper I) contained in each event data.

The PIN event data, sent from HXD-AE to HXD-DE, contain cosmic-ray produced saturated events at a rate of $\sim 10\,\mathrm{ct\,s^{-1}}$ per one well unit; these can be easily removed by using the PIN-UD flag. In addition, the electric interference from the satellite power line was observed in some units, at a rate up to $\sim 100\,\mathrm{ct\,s^{-1}}$. Since the interference-produced events appear as common-mode noise among neighboring PIN diodes, they can be eliminated in HXD-DE based on multiple triggers among the four PIN diodes in the same well unit; that is, PIN events with single trigger are out to the telemetry. Finally, tighter lower threshold levels are digitally applied to individual PIN signals, to remove thermal noise events with low pulse heights. This "digital LD", ranging over 16–32 ADC channels, can be individually applied by commands to the 64 PIN pulse-heights, whereas the analog LD in HXD-AE is common among the sixteen PIN diodes in the same WPU module. As a result, the average of the summed event rate from 64 PINs is ordinarily reduced down to 6–10 $\mathrm{ct\,s^{-1}}$, although there still remains a rapid increase up to $40\,\mathrm{ct\,s^{-1}}$ during the daytime of the satellite.

To suppress the GSO event rate, a tighter setting in the PSD cut condition is inevitable, because the digitized "GSO" data actually contain a large number of BGO events, particularly at the lower energy end. As shown in figure 2, individual trapezoids are defined on the fast–slow histograms, to discard the residual BGO branch. These boundaries, called "digital PSD" hereafter, at the same time eliminate events with too low or too high pulse heights, corresponding to a digital lower and upper discriminator at $\sim$ 30 keV and $\sim$ 700 keV, respectively. The summed GSO event rate from the 16 well units is thus reduced to 70–150 ct s^{-1}, which varies according to the satellite position in the orbit (subsection 5.2). In table 4, the counting rate reduction of PIN and GSO by each stage of cut in HXD-AE, HXD-DE, and analysis software (subsections 3.3, 4.4, and 4.5) is summarized.

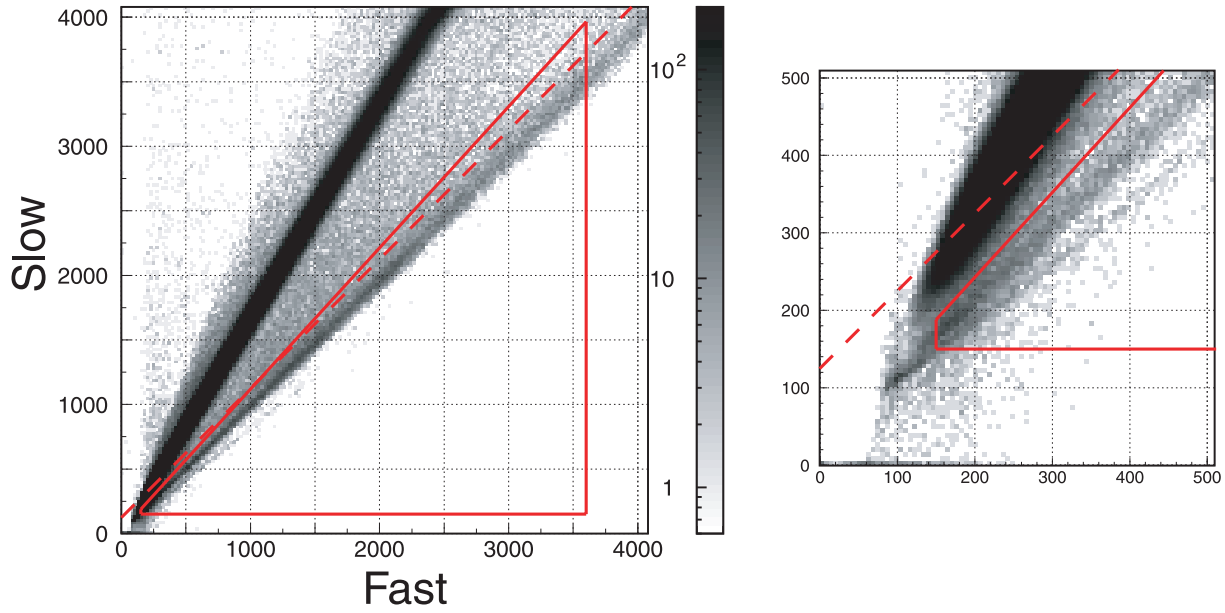

Fig. 2. Digital PSD selection criteria (solid trapezoid), shown on a two-dimensional histogram of fast and slow-shaped pulse heights, obtained while the hard-wired PSD function is disabled. The dashed line denotes the hard-wired PSD cut.

Table 4. Counting rate of PIN and GSO at each stage of cut.

	PIN ($\mathrm{cts^{-1}\,unit^{-1}}$)*	GSO ($\mathrm{cts^{-1}\,unit^{-1}}$)*
HXD-AE		
Initial analog LD rate	10–100	700–1000
After analog PSD cut	···	< 100
HXD-DE		
After PIN UD cut	1–100	···
After single PIN trigger cut	1–10	···
After digital LD	0.4–2.5	···
After digital PSD	···	5–10
Analysis software†		
After anti-coincidence applied	0.025–0.075	1.5–2.5

* Counting rate per a well unit.
† Described in subsections 3.3, 4.4, and 4.5.

2.5. *Operation History*

After the initial run-up operation, the parameters of HXD-AE and the event selection conditions in HXD-DE have been basically kept unchanged throughout the performance verification phase, except for some minor adjustments, summarized in table 5. In addition, the nominal observation of HXD was an interrupted few times for the purpose of a memory dump operation of HXD-DE, to investigate any unexpected status errors in-orbit.

An ordinary daily operation of the HXD includes a fixed sequence of health checks, resetting counters, and outputting diagnostic information. In the nominal observation mode, the hardware and software settings are optimized to reduce the detector background as much as possible. However, background events are still useful for diagnostic purposes. Therefore, by utilizing Earth occulted periods in the orbit, the PSD selection in both HXD-AE and HXD-DE are disabled for 10 minutes every day, to monitor the BGO events from individual well units. At the same time, the digital thresholds of PIN events are also disabled to obtain noise spectra from individual PIN diodes. Therefore, a much higher event rate than the maximum transfer rate saturates the telemetry during this period, and prevents the instrument from performing any scientific observation.

Each WPU module has time counters to record latched values on each triggered event. These counters are simultaneously reset at the beginning of each observation by programmed commands. Counters for LD and UD are reset at the end of every SAA passage to restart the anode LD counters, which sometimes "freeze" due to a bug of digital logic in WPU.

Table 5. Major operations of the HXD during the first one year.

Date	Operation
Sep 17	HXD-AE RBM level raised: 10 kHz → 100 kHz
Oct 22	HXD-DE memory dump
Nov 16	HXD-S control temperature raised: −20 °C → −14.5 °C
Dec 30–Jan 4	PMT-HV reduced to 0 V
Mar 20	WAM time resolution changed: 1.0 s → 0.5 s
Mar 22	HXD-S control temperature lowered: −14.5 °C → −20 °C
Mar 23	GSO anode LD lowered: 40 mV → 30 mV
	Digital PSD range changed: 150–3600 → 120 ch–3000 ch
	Telemetry rate at Bit-M changed: 33 kbps → 44 kbps
Mar 27	Digital PSD range changed: 120–3000 → 100 ch–3000 ch
Apr 15	Telemetry rate at Bit-L changed: 10 kbps → 15 kbps
May 13	GSO anode LD raised: 30 mV → 40 mV
May 17	HXD-DE memory dump

2.6. Data Processing

Both scientific and house-keeping data are immediately recorded in an onboard data recorder, and later transmitted to the ground tracking stations as raw telemetry packets. These data are promptly transferred to storages at the data center of ISAS/JAXA, and converted into the Flexible Image Transport System (FITS, Wells et al. 1981) data format. Standard pipeline processings are then applied, which consist of following data handlings with the relevant software (FTOOLS, Blackburn 1995). Throughout this paper, we have used pipeline products, processed with a set of softwares and calibration files tagged as a version 1.2.[1]

First, the absolute timing is assigned by `hxdtime`, relying on time record of 19 bits length and 61 μs precision (Paper I) in individual events, and on coarse timing information contained in a header block of event data packets. An absolute time for each event is obtained by homologizing the time record to the original clock in the satellite digital processor, and then synchronizing it to the standard oscillator on the ground. Transmission delays and temperature drift of the onboard clock are also taken into account in this process. In the next step, the pulse-heights of each event are transformed by `hxdpi`, from analog-to-digital converter (ADC) channels into pulse-height invariants (PI), which is linearly proportional to the physical energy of incident photons. The energy range and channel numbers of PI are commonly defined as 0.375–96.375 keV with 256 channels for PIN events, and as 1–1025 keV with 512 channels for GSO events. In the case of PIN events, fixed conversion factors are applied on the 64 pulse-heights to obtain the proper energy scale, using the in-orbit calibration (subsection 3.1) and non-linearity corrections in HXD-AE. On the other hand, in the case of GSO events, due to temperature-dependent PMT gain changes, time-dependent conversion factors are applied by in-orbit calibration lines (subsection 4.1) to obtain the proper energy scale. Finally, events are qualified by `hxdgrade`, based on the trigger patterns, hit-pattern flags, and various quality information recorded by HXD-DE (Paper I). The selection criteria optimized for the PSD selection (subsection 4.4) and anti-coincidence (subsection 3.3, subsection 4.5) are also applied, and events that pass all of these cuts are tagged as "clean events".

[1] ⟨http://www.astro.isas.jaxa.jp/suzaku/process/history/v1223.html⟩.

3. In-Orbit Performance of PIN

In-orbit calibrations of the PIN diodes have been carried out in three steps. First, for each of the 64 PINs, the absolute energy scale is established, the energy resolution (subsection 3.1) is evaluated, and the lower energy threshold (subsection 3.2) is optimized. Second, the event selection criteria is optimized so as to minimize the residual non X-ray background (subsection 3.3). Finally, the response matrices of individual PINs are constructed, based on the quantum efficiencies and effective areas (subsection 3.4).

3.1. Energy Scale

Before launch, the energy scales of the 64 PINs were precisely measured using the standard γ-ray sources, within $\sim 1\%$ accuracy (Paper I). These energy scales, or gains, are not expected to significantly change after the launch, since neither the charge collection efficiency of the PIN diodes nor the capacitance of the charge-sensitive amplifiers is sensitive to environmental changes. Nevertheless, the energy scale is so important that it should be accurately reconfirmed using actual data. Instead of calibration isotopes, fluorescent X-rays from gadolinium (Gd Kα 42.7 keV) and bismuth (Bi Kα 76.2 keV) in GSO and BGO scintillators, respectively, can be used for in-orbit energy scale calibrations. These fluorescent events are hardly detected in "clean events", because they are eliminated by anti-coincidence with the scintillator signals, caused by simultaneous energy deposits. Consequently, as shown in figure 3, they can be extracted with a high signal-to-noise ratio by selecting only coincidence events between PIN diodes and scintillators of the same well unit.

As shown in figure 3, by fitting the pulse-height spectra with four Gaussian profiles, which represent the Kα_1, Kα_2, Kβ_1 + β_3, and Kβ_2 transition lines and a background continuum, the peak channels of the Kα_1 line were obtained

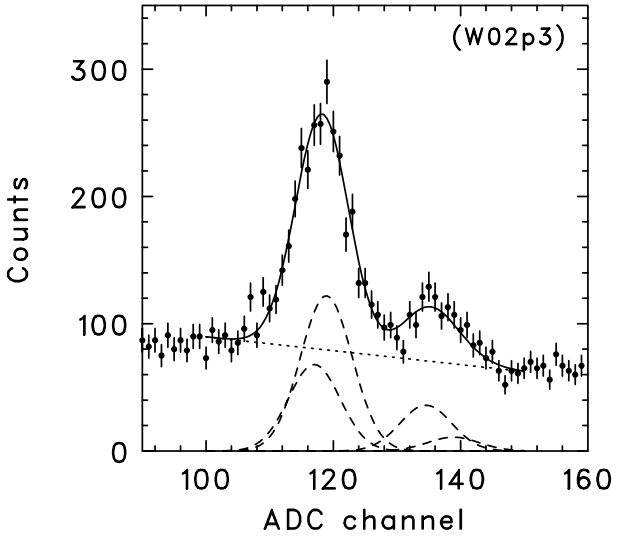

Fig. 3. Energy spectrum of a single PIN diode, in which the coincident events of PIN and GSO are accumulated over a half year. Four Gaussian profiles indicated by dashed lines, correspond to the Kα_1 (43.0 keV), Kα_2 (42.3 keV), Kβ_1 + β_3 (48.6 keV), and Kβ_2 (50.0 keV) fluorescence lines of gadolinium, while the linear component shown by the dotted line denotes a background continuum.

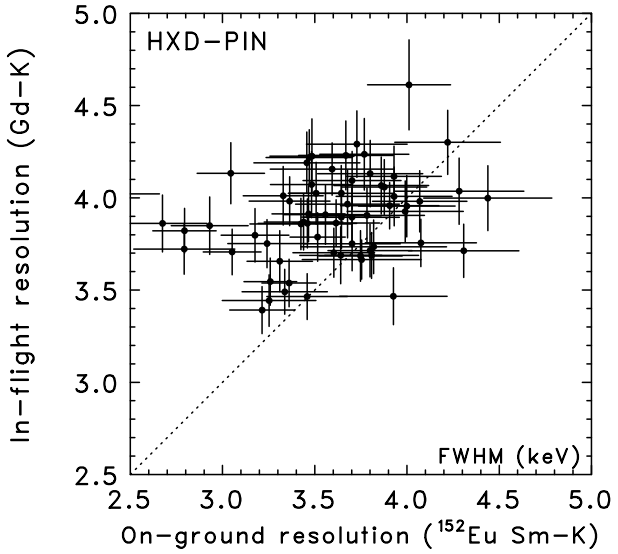

Fig. 4. Comparison between the energy resolutions of the PIN diodes measured on-ground and in-orbit, by use of the ^{152}Eu isotope (Sm Kα_1: 40.1 keV) and the Gd Kα_1 (43.0 keV) line, respectively.

for individual PINs, and the energy resolution of that peak was measured at the same time. In this fitting, the four Gaussian centroid energies were constrained to obey theoretical line-energy ratios, and the Gaussian widths were tied together but left a free parameter. In figure 4, the thus-obtained energy resolutions of the 64 PINs are plotted against those measured in the pre-launch calibration. The typical in-orbit energy resolution for the Gd Kα line was obtained as ~ 4 keV in FWHM, which is roughly consistent with those measured before the launch. A slight increase of ~ 0.3 keV from the pre-launch

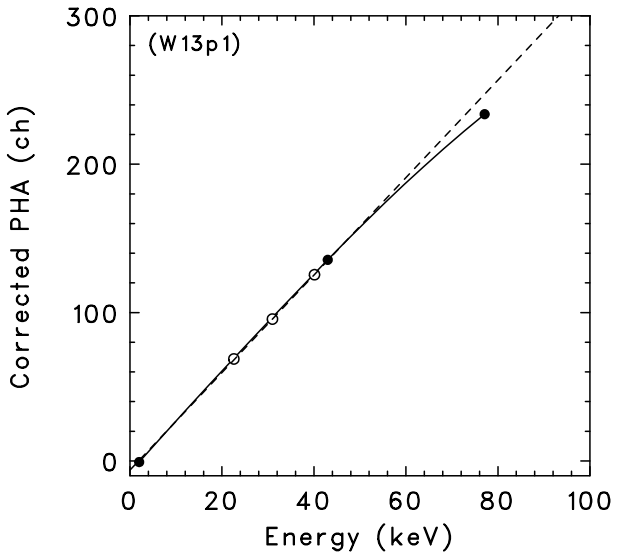

Fig. 5. Energy vs. pulse-height linearity of a representative PIN diode. The open and filled circles represent the on-ground and in-orbit calibration points, respectively. The solid line indicates the spline curve obtained with the in-orbit calibration points, while the dashed line shows the linear energy scale determined with the on-ground measurements. The pulse height is shown in units of the pulse-height amplitude (PHA), which is equivalent to the ADC channel after a correction of nonlinearity in HXD-AE.

resolutions are probably due to a difference in the electrical noise conditions.

In addition to the two fluorescent lines, another anchor point is needed at low energies to accurately fix the energy scales. For this purpose, the "*pedestal channel*", which is defined as the peak channel of the noise spectrum obtained by random triggers from scintillators, is used. Although the energy deposits to the relevant PIN diode are considered in this case to be essentially zero, the channel becomes non-zero, because the peak-hold circuit before ADC latches the noise peak during each trigger gate of a $\sim 10\,\mu$s width. Therefore, the pedestal channel of each PIN is thought to be proportioned to its energy resolution. Based on ground measurements using "flight equivalent" PIN diodes and analog electronics, an energy resolution of ~ 4 keV yields a pedestal channel of ~ 2 keV. Therefore, the measured pedestal channel of each PIN diodes is assigned to an energy of 2.0 keV. Finally, as shown in figure 5, a spline curve is derived over an energy range of 2–76 keV for each PIN diode using the three calibration points. The accuracy of this scale is estimated to be about 1%, based on deviations of the calibration points from the spline curves. The in-orbit energy scales agree well with the pre-launch ones measured in an energy range of 20–50 keV, while some PINs show significant nonlinearities above 50 keV.

The average counting rate of the background Gd K line is $\sim 1.2 \times 10^{-4}\,\mathrm{ct\,s^{-1}}$ for one PIN. Therefore, long-term variations of the individual gains can be monitored when accumulated over one to two months. As shown in figure 6, the PIN gains have stayed constant, within one ADC channel (~ 0.4 keV), at least for half a year. Therefore, throughout the performance verification phase, each PIN diode employs

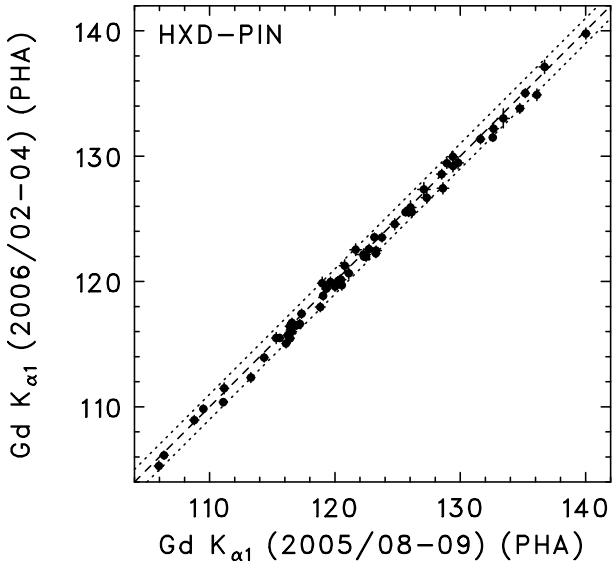

Fig. 6. Comparison of the Gd K peak channels of the 64 PINs between two periods that are 1–2 and 7–9 months after the launch.

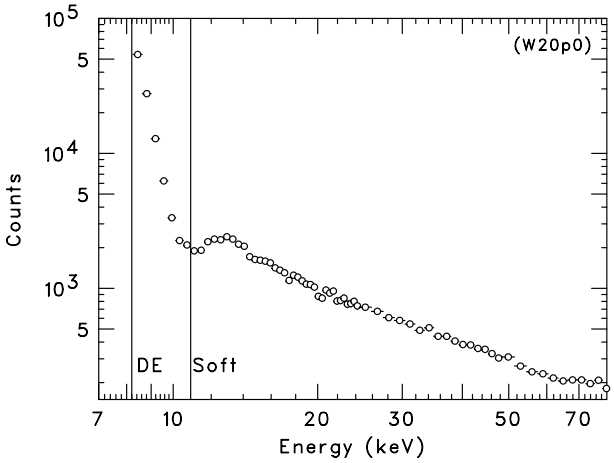

Fig. 7. Typical background spectrum of one PIN. Two vertical lines indicate the LD level applied in HXD-DE, and the energy threshold used in the processing software.

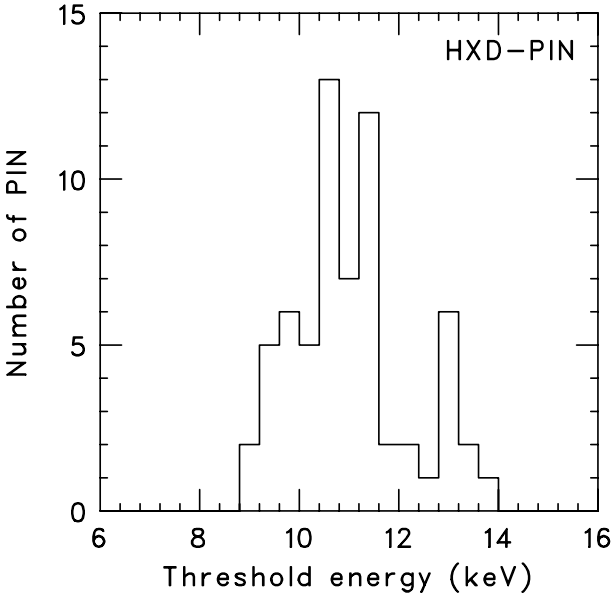

Fig. 8. The number histogram of energy thresholds of the 64 PIN diodes.

a single energy scale of its own when converting the raw ADC channels into the pulse height invariants (PI).

3.2. Energy Threshold

As previously described in subsection 2.3 and subsection 2.4, the PIN signals are screened by the onboard analog and digital lower discriminator (LD) levels, in HXD-AE and HXD-DE, respectively. However, the PIN events transmitted to ground still contain a low-energy thermal and/or electrical noise component, which varies significantly in orbit. To remove these noise events, a higher threshold must be applied by the analysis software (subsection 2.6) to individual PIN diodes. As shown in figure 7, this "software LD" was set at the crossing point between the noise spectrum and non-celestial background events. A long-term stability of the noise spectrum was also confirmed from a comparison of screened spectra obtained in 2005 September and 2006 February (Fukazawa et al. 2006). Combined with the energy scale, this software LD determines the actual lower-limit energy of the relevant PIN diode. Figure 8 shows the distribution of the energy thresholds determined in this way. It ranges from 9 to 14 keV, with an average of ~ 10 keV, which satisfies the design goal. After event screening by these thresholds, each spectrum loses its effective area below the corresponding energy, and this effect should be correctly taken into account in the energy response matrix for PIN.

3.3. Background Reduction

After discarding the low-energy events below the individual thresholds set by the data-analysis software, the residual background of the PIN diodes is further reduced by fully utilizing the anti-coincidence method, which comprises the basic concept of the HXD. Before applying anti-coincidence, a typical summed event rate from all of the 64 PIN diodes is already reduced down to 2–3 ct s^{-1}, about one percent of the initial trigger rate, most of which are caused by in-orbit electrical interference or thermal noise. Figure 9 illustrates how the PIN background is reduced by the stepwise application of anti-coincidence conditions. In the figure, the crosses denote events that were extracted from a period when the PMT high-voltages were reduced to zero due to operational reasons, that is, when the BGO shields were working only as "passive" shields and collimators, rather than the active anti-coincidence counters. This background level is as high as those achieved in past hard X-ray missions equipped with passive collimators (Rothschild et al. 1998; Frontera et al. 1997). Once the BGO shields start working and the hard-wired PSD function is enabled (i.e., events with significant energy deposits onto BGO are discarded in HXD-AE), the background decreases by a factor of 3, as indicated by the open triangles in figure 9.

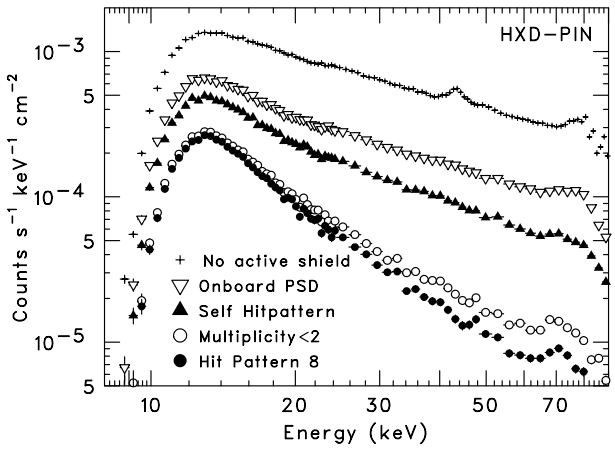

Fig. 9. Background spectra summed over the 64 PINs, acquired under various reduction conditions (see text). They are normalized by the total geometrical area of the 64 PIN diodes.

Since the threshold energy for the PSD is higher than that for hit-pattern generation, the remaining events can be almost halved through on-ground data screening, by discarding those events that carry the hit-pattern flag from the same unit (filled triangles).

The whole detector volume of HXD is always exposed to energetic cosmic-ray particles, of which the energies are higher than the geomagnetic cut-off rigidity (COR) of several GV, with a typical flux of ~ 1 particle s^{-1} cm^{-2}. When they penetrate the detector, secondary radiation is promptly generated, which adds to the background events in surrounding units. Since most of the cosmic-ray particles are charged, their penetration usually causes simultaneous hits to multiple units. This "multiplicity", N, defined by the hit-pattern signals, can be used as an efficient tool for the rejection of such events. Here, a valid PIN or GSO event is defined to have a multiplicity of N ($0 \leq N \leq 35$), if there are simultaneous hits in N units, excluding the relevant triggering unit, itself. If a smaller multiplicity is required as the screening condition, the background will become lower, but the signal acceptance will also decrease due to an increase in the accidentally coinciding probability. With an average counting raw rate of ~ 1 kct s^{-1} in each unit and a coincidence width of 5.6 μs, requiring $N \leq 1$ has been found to be optimum; that is, events are discarded if there are two or more hits in the hit-pattern, except that from the triggering unit, itself. This condition leads to a further background reduction by a factor of three, as represented by the open circles in figure 9.

Although applying a tighter multiplicity cut, i.e., requiring $N = 0$ (no hit in any other unit) is unfavorable because of a reduction in the signal acceptance, the $N = 0$ requirement works effectively if used under appropriately restricted conditions. In fact, the filled circles in figure 9 represent the spectrum obtained by requiring $N = 0$ in the surrounding 8 units around the triggering one. Detailed studies confirm that this condition (and $N \leq 1$ in the remaining 27) optimizes the anti-coincidence condition (Kitaguchi et al. 2006). The final background event rate obtained after applying all of these screening conditions is reduced to a mere ~ 0.5 ct s^{-1}, which corresponds to $\sim 3 \times 10^{-4}$ ct s^{-1} keV^{-1} cm^{-2} at 13 keV, and $\sim 1 \times 10^{-5}$ ct s^{-1} keV^{-1} cm^{-2} at 60 keV, for a geometrical area of 174 cm^2.

3.4. Energy Response

Using Monte Carlo simulations based on the GEANT4 toolkit (Allison et al. 2006; Agostinelli et al. 2003; Terada et al. 2005), and implementing therein the same event screening conditions as those employed by the analysis software, energy response matrices can be constructed individually for the 64 PIN diodes. Geometrical parameters, such as the size of the guard-ring structure of the PIN diodes (16.5 mm $\times$ 16.5 mm; Paper I), or individual inclinations of the fine-collimators measured in orbit (subsection 6.1), are precisely described in a "mass model", together with the chemical composition of the material. In-orbit calibration results, such as the energy scales, energy resolutions, and spectral shapes set by the analog LD, which were individually measured using the Crab spectra, are also imported into the Monte Carlo simulation.

The silicon PIN diodes used in the HXD are so thick, ~ 2.0 mm, that their full depletion needs a bias voltage of around 700 V (Ota et al. 1999). Therefore, at the nominal operation voltage of ~ 500 V, the actual thickness of the depletion layer can vary among the 64 PINs, and should be individually calibrated. This was done according to the following two steps. First, the Crab spectrum of each PIN was analyzed for its slope in an energy range of 45–78 keV, where the diode thickness has little effects. The slope was determined solely by the Crab's slope and the energy dependence of the interaction cross-section of silicon. This analysis confirmed that the energy scales established in subsection 3.1 are correct. Then, the overall 15–78 keV Crab spectra were fitted individually by a single power-law model, and the effective thickness was adjusted so that every PIN spectrum can be reproduced by the same photon index as obtained in the 45–78 keV band. Finer tunings were introduced to properly model the shape of the efficiency decrease toward lower energies, which is mainly determined by the 64 analog LD levels. Finally, by combining the 64 response matrices into a single one, 64-PIN summed spectra can be collectively examined.

Since Suzaku has two nominal pointing positions, ("XIS nominal" and "HXD nominal"), two corresponding response matrices were constructed (`ae_hxd_pinxinom_20060814.rsp` and `ae_hxd_pinhxnom_20060814.rsp`). Figure 10 shows the Crab spectra (64 PINs summed) measured at these two nominal positions. There, blank-sky backgrounds, obtained two days before, were subtracted. The spectra were then fitted with a single power-law model, using the relevant response matrix over an energy range of 12–70 keV; the obtained best-fit parameters are summarized in table 6. Thus, the spectrum is well reproduced within a few percent over the entire range used, while the deviation becomes larger up to 10% below ~ 12 keV, where the effective area is rapidly changing with the energy. There is also an artificial structure at around the characteristic X-ray energy of gadolinium, suggesting that the modeling of the effect of active shields is yet to be improved.

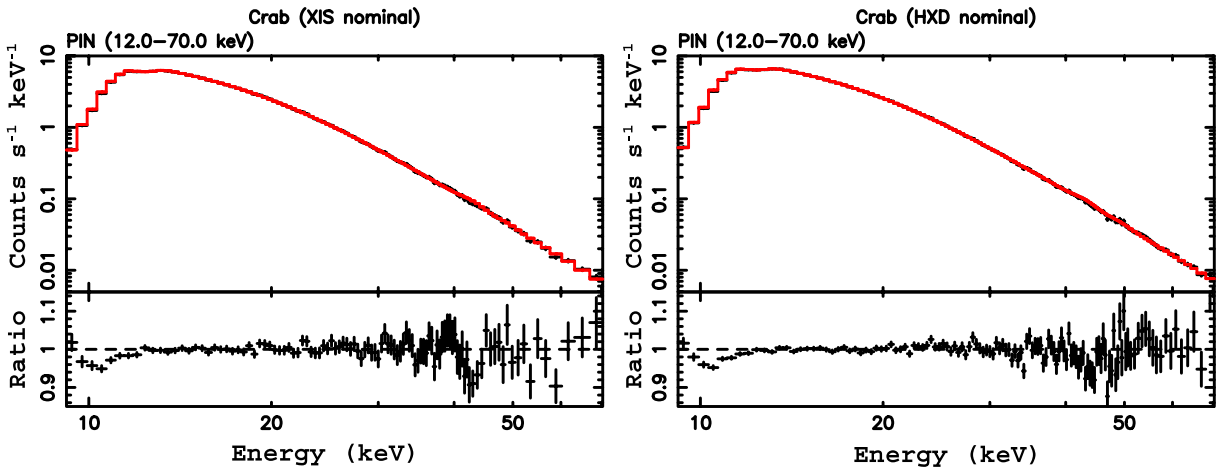

Fig. 10. Background-subtracted HXD-PIN spectra (64 summed) of the Crab Nebula, obtained at the XIS nominal (left) and HXD nominal (right) positions, compared with predictions (red) by the best-fit power-law model, of which the parameters are given in table 6. The fitting was carried out in the range of 12–70 keV, and then remaining channels were retrieved. The lower panels show the data-to-model ratio.

Table 6. Best-fit parameters and 90% confidence errors for the PIN spectra of the Crab Nebula.*

Target position	Photon index	Normalization†	χ^2_ν (d.o.f)
XIS nominal‡	2.11 ± 0.01	11.7 ± 0.14	1.03 (152)
HXD nominal§	2.10 ± 0.01	11.2 ± 0.09	1.24 (152)

* The column density for the interstellar absorption is fixed at 3×10^{21} cm^{-2}.
† Power-law normalization in units of photons cm^{-2} s^{-1} eV^{-1} at 1 keV.
‡ Observation performed on 2005 September 15 19:50–September 16 02:10 (UT).
§ Observation performed on 2006 April 05 12:47–April 06 14:13 (UT).

4. In-Orbit Performance of GSO

4.1. Energy Scale

The pulse heights of GSO events depend on the light yields of the individual scintillators, the PMT gains, which are sensitive functions of the high voltage levels, and the amplifier settings in HXD-AE (table 3). Among these factors, the scintillator light yields and the PMT gains are temperature sensitive. Before launch, the GSO pulse heights in the 16 well units were roughly equalized by adjusting the high-voltage levels (per 4 well units), and trimming resistors in the high-voltage distribution boxes. However, the GSO pulse heights for a given energy changed across the launch (subsection 2.3), and have been changing since then, due, e.g., to the HXD-S temperature fluctuations (subsection 2.1), and to some unit-dependent long-term and short-term effects (to be detailed in subsection 4.3), which are most likely taking place in the PMTs. The GSO pulse heights must be corrected for these temporal gain changes in order for them to be correctly converted to energies. At present, the gain parameters in HXD-AE are kept fixed to the values reached through the initial operation (subsection 2.3), so as to maintain consistency of the calibration data base.

The in-flight GSO energy scales (i.e., the relations between the incident photon energies and the output pulse heights), including the temporal gain changes mentioned above, can be determined utilizing several nuclear lines in the background spectra. One is the broad line feature at ~ 350 keV with a count rate of ~ 0.16 ct s^{-1} per well unit (Paper I), produced by α particles from a natural radioactive isotope, ^{152}Gd, contained in GSO. Extensively utilized in the pre-launch calibrations, this broad line also provides a good in-orbit calibrator, because it is clearly detected in the background spectra, as shown in figure 11; under the full anti-coincidence condition (subsection 4.5), this feature can be detected in 2–3 ks of data integration.

In addition to the ^{152}Gd peak, proton-beam irradiation experiments, conducted before launch using accelerator facilities (Kokubun et al. 1999), predict several radioactive isotopes to be created in GSO, by high-energy particles including geomagnetically trapped protons in the SAA. These "activation" isotopes, generally proton-rich, decay via either β^+ or electron-capture (EC) processes. While β^+-decay species produce continuum, and are hence useless for calibration purposes, the EC process will give a full energy deposit in GSO, and will-produce spectral lines with well-defined energies. As shown in figure 11, several peaks appeared in the GSO background spectra under the full anti-coincidence condition (subsection 4.5), and were successfully identified with the corresponding isotopes, as listed in table 7. The most prominent line, at ~ 150 keV, is due to EC decay of ^{153}Gd. Since this isotope has a half-life of 241 days, the line has been gradually building up after the launch on a similar time scale (subsection 5.3). As of 2006 January, it has an average counting rate of

Table 7. Activation lines used for in-orbit calibration of the GSO energy scale.

Energy (keV)	Radioactive isotope	Decay mode	Half life
70.0	^{151} Gd	EC	124 (d)
153.0	^{153} Gd	EC	241 (d)
196.0	^{151m}Eu	IT	60 (μs)
$\sim$ 357	^{152} Gd (natural)	α	1.1×10^{14} (yr)
511.0	various	β^+	

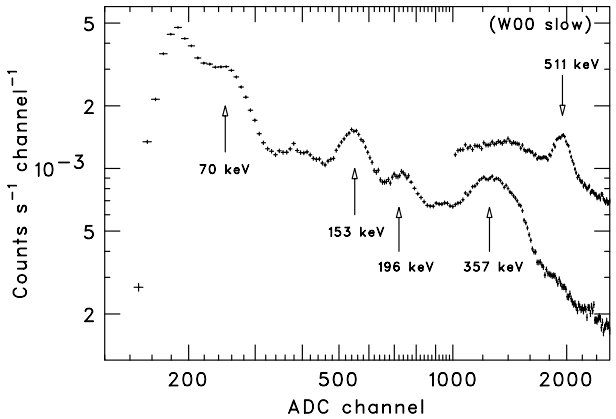

Fig. 11. Typical phoswich pulse-height spectra of one well unit, acquired in orbit from the blank sky. The lower data points represent events obtained in the full anti-coincidence condition, while the higher ones, shown only above 1000 channels for clarity, indicate those discarded by anti-coincidence.

~ 0.05 ct s^{-1} per well, and can be used as a second calibrator.

Proton-induced activation takes place not only in GSO, but also in the surrounding BGO shields. Subsequent β^+-decay events in BGO are usually detected as "multi-hit" events, because each of them produces a pair of annihilation photons at 511 keV, which are generally detected by neighboring units. Although these events are rejected in normal observations by anti-coincidence, the 511 keV peak is clearly detected, as shown in figure 11, if such multi-hit events are purposely accumulated. By fitting these pulse-height spectra, in-orbit energy resolutions of individual well units, at $\sim$ 500 keV, were measured and confirmed to be almost the same as those obtained on-ground calibrations ($\sim$ 11%, Paper I). The annihilation line intensity decreases rapidly after each SAA passage, on a typical time scale of $\sim$ 10 ks, resulting in a day-averaged rate of ~ 0.1 ct s^{-1} per well unit.

Thus, the in-orbit data contains at least three peaks with secure energy identifications of 511 keV, 350 keV, and 153 keV. By fitting them with a linear function, the first approximation to the GSO energy scales of the individual well units was obtained as

$$P = a_i E - b_i. \quad (1)$$

Here, E is the photon energy in keV, P is the pulse height in units of ADC channels, $a_i \sim 4$ channel keV^{-1} and $b_i \sim 50$ channels are positive parameters, and $i = 0, 1, \ldots, 15$ is the unit number.

4.2. *Corrections for Nonlinearity*

The offsets $-b_i < 0$ in equation (1) are due to nonlinearities, both in the GSO light yields and the HXD-AE performance, which are known to become significant at energies below $\sim$ 100 keV (Uchiyama et al. 2001; Kawaharada et al. 2004; Paper I). Therefore, equation (1) is thought to be accurate only at energies above 150 keV. If, in fact, equation (1) is tentatively extrapolated to below 150 keV, it underestimates the pulse height of another emission line seen in the data, namely the 70 keV line originating from EC-decays of ^{151}Gd (table 7). As a result, all well units were reconfirmed to show the expected nonlinearities with the same sense as indicated by the negative offset $-b_i$, but with larger deviations ($\sim$ 10% at 70 keV) than were measured in the on-ground calibrations ($\sim$ 3%).

In order to represent the nonlinearity, equation (1) has been improved empirically as

$$P = a_i E - b_i + c_i \exp(-E/d_i), \quad (2)$$

where $c_i \sim 280$ channels and $d_i \sim 35$ keV are additional positive parameters. The values of c_i and d_i were determined using the activation peak at 70 keV and the K-edge energy of gadolinium (50 keV, subsection 5.3), and also requiring the pulse heights for $E = 0$ (namely $P = -b_i + c_i$ channels) to coincide with the "pedestal" ADC channels (subsection 3.1), which are measured in orbit by inspecting events triggered by any one of the four PIN diodes.

As shown in figure 12, the empirical energy scales of equation (2) have been confirmed to account for the employed calibration features within $\pm$3%, in every unit, over the entire energy range from 50 to 600 keV. An independent confirmation of equation (2) has been obtained from comparisons between the PIN and GSO spectra of two X-ray pulsars with cyclotron absorption lines at around 35–45 keV (Terada et al. 2006).

4.3. *Temporal Gain Changes*

Figure 13 shows long-term GSO gain histories of several representative well units, determined referring to the pulse heights of the 511 keV line, which has the highest signal-to-noise ratio among the available calibrators. Each data point in these histories represents the average over an observation, which lasts typically one to two days. Over the first 9 months in orbit, all the well units have thus exhibited gradual gain decreases, by 5% (minimum) to 20% (maximum). In addition to the long-term trends, figure 13 also reveals short-term gain fluctuations, which are anti-correlated with the temperature

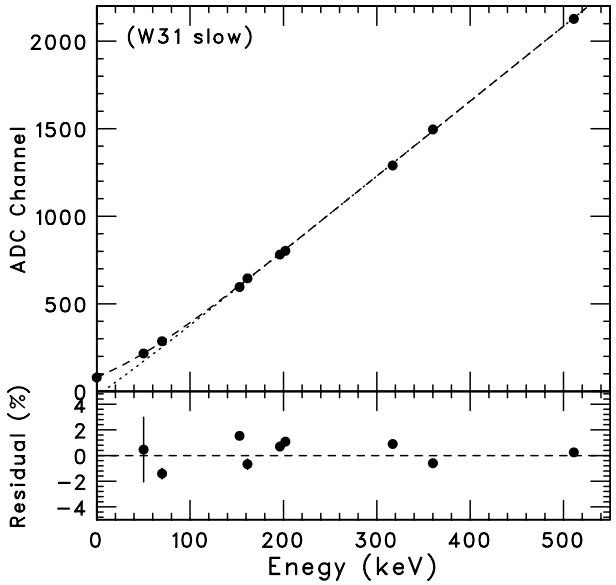

Fig. 12. Energy scales of GSO in a particular well unit, determined with equation (1) (dotted line) and equation (2) (dashed curve), fitted to various energy-scale calibration features. The lower panel shows residuals from the dashed curve.

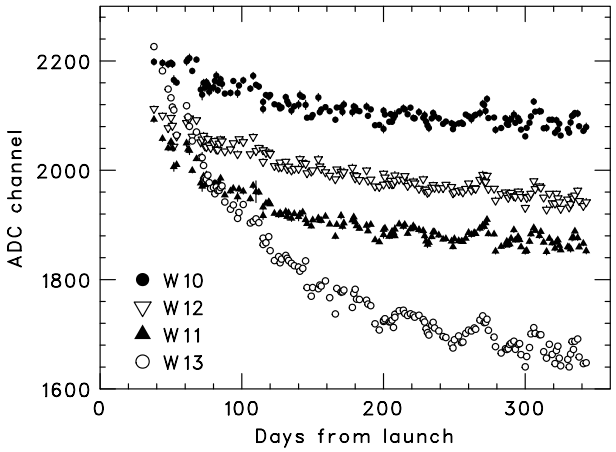

Fig. 13. Long-term variations of the GSO gains in four well units, which are biased by the same high-voltage supplier, determined in reference to the 511 keV line, from 2005 September to 2006 May.

history of figure 1. This is because the GSO light yield and the PMT gain both depend inversely on the temperature, with typical coefficients of $\sim 0.5\%$ C^{-1} and $\sim 0.2\%$ C^{-1}, respectively.

Figure 14 represents a short-term gain history of a particular well unit, constructed by accumulating its GSO events into a series of spectra every 2 ks, and fitting the 511 keV line therein. It reveals a periodic variation by a few percent on a yet shorter time scale than that of the temperature fluctuation, synchronized with the orbital revolution of Suzaku (~ 96 min). This is because the PMT gains jump up slightly when the high voltages are resumed after spending the off period in the SAA, and then gradually decrease in somewhat unit-dependent

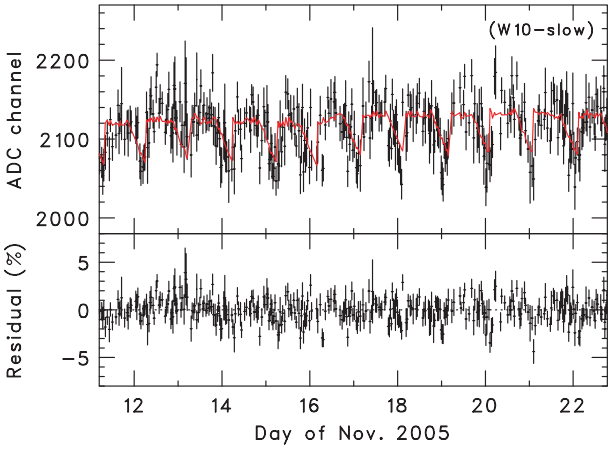

Fig. 14. Short-term GSO gain variations in a representative well unit, measured every 2 ks during ~ 10 days in 2005 November. The top panel shows peak channels of the 511 keV line and the prediction of an empirical model (red), while the bottom panel shows deviations from the model.

ways. Therefore, the gains show almost stable levels in "SAA orbits" that contain the high-voltage resets, whereas they continue to decline in "non-SAA orbits" until the next reentry. This behavior is modeled by an empirical function in terms of the measured temperature of HXD-S and the time after high-voltage resumption (Fukazawa et al. 2006). The model parameters are adjusted, unit by unit, by fitting the actual gain histories. As exemplified by red curves in figure 14, the model can reproduce the instantaneous GSO gains, namely the parameter a_i in equation (2), to an accuracy of 3% as a function of time with a typical time resolution of 2 ks.

4.4. Background Reduction with PSD

As described in subsection 2.4, the HXD events are normally transmitted to ground after being first screened by the hard-wired PSD in HXD-AE, and then by the digital PSD in HXD-DE. Nevertheless, the data still contain significant background events, namely residual BGO events at lower energies ($\lesssim 100$ keV), and residual Compton events at higher energies. In order to achieve the highest sensitivity to celestial signals, the PSD criteria must be further tightened and optimized in off-line data analyses, by discarding these background events as much as possible, but retaining the signal acceptance. This process is hereafter called "software PSD".

In order to find the optimum software PSD condition, Kitaguchi et al. (2006) analyzed the two-dimensional fast–slow diagram (Paper I) of the Crab Nebula, unit by unit, after subtracting blank-sky backgrounds. They quantified the Gaussian-equivalent "spread", $\sigma(E)$, of the GSO events on the diagram in the direction ($-45°$), which is perpendicular to its branch. As shown in figure 15, the obtained width of the GSO branch, as a function of the energy, shows a good agreement with those measured on the ground above 150 keV, while being slightly broadened at the lower energy range, probably due to an in-orbit nonlinearity effect of the PMTs (subsection 4.2). Then, the Crab Nebula data and the blank-sky background were screened in the same manner, using $\pm x\,\sigma(E)$ cuts where $x > 0$

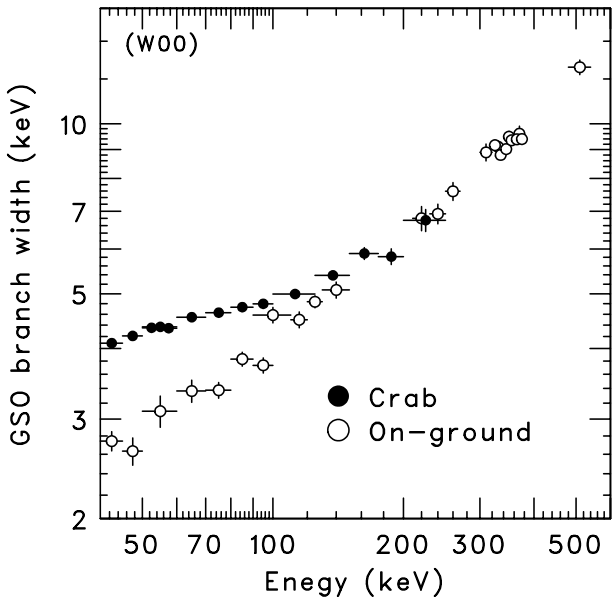

Fig. 15. GSO branch width (Gaussian sigma) on the fast–slow diagram, shown as a function of energy. The open black circles indicate pre-launch measurements using isotopes, while the filled circles refer to the Crab Nebula data after background subtraction.

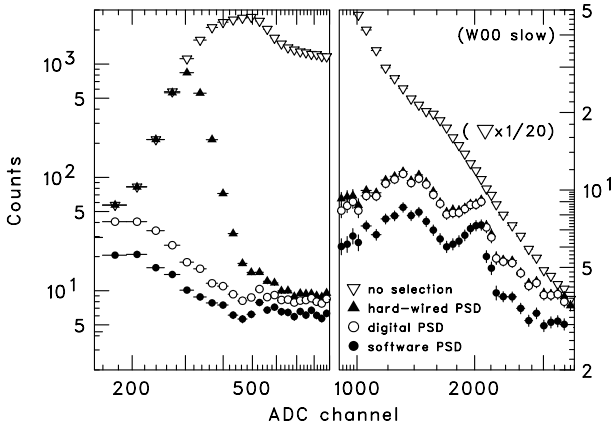

Fig. 16. Raw in-orbit background spectrum of a well unit without any PSD selection, compared with those after applying the hard-wired, digital, and software PSD selections. Data were integrated during daily diagnostic runs, when the onboard PSD function is temporarily switched off (subsection 2.5). The spectra are shown separately below and above 900th channel in the left and right panels, respectively. For clarity, the raw background spectrum in the right panel is reduced in intensity by a factor of 20.

is the cut condition to be optimized. By examining how the residual blank-sky background and the Crab signals change with x, it was found that $x = 2.1$, which corresponds to a signal acceptance of 96%, generally maximizes the signal-to-noise ratio under background-dominant conditions. Through this optimum software PSD cut, the GSO background data transmitted to ground has been further reduced by 50%, as illustrated in figure 16.

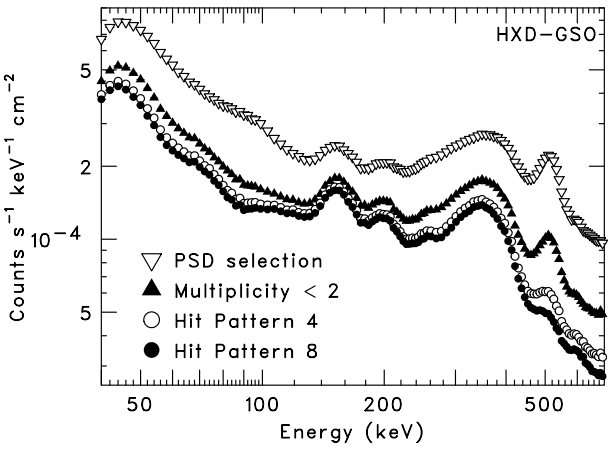

Fig. 17. Background spectra summed over the 16 well units, acquired under various anti-coincidence conditions (see text). They were normalized by the total geometrical area of the 64 GSO scintillators.

4.5. *Background Reduction with the Anti-Coincidence*

After applying the software PSD within each well unit, the GSO background, like the PIN data, can be further reduced using the anti-coincidence function working among multiple well and anti units. This screening is particularly useful in eliminating secondary radiation produced by cosmic-ray charged particles, and the 511 keV lines originating from β^+ decays of activated nuclei in the BGO shield (subsection 4.1). However, like the PSD case, too severe anti-coincidence conditions would reduce the signal acceptance via chance coincidence; accordingly, the conditions need to be optimized.

As detailed in Kitaguchi et al. (2006), the optimum anti-coincidence condition has been found to reject a GSO event (surviving the full PSD cut) from a well unit as backgrounds, if either of the following two conditions are satisfied:

1. It has a simultaneous hit in at least one of the 8 units that surround the relevant well.
2. It has at least two simultaneous hits in any units other than the relevant unit itself.

As shown in figure 17, applying this condition has nearly halved the GSO background over the entire 50–500 keV range. In particular, the 511 keV lines have been reduced to a level of $\sim 0.05\,\mathrm{ct\,s^{-1}}$, because most of them are emitted in pairs from β^+-decay nuclei, and hence they produce double hits. The measured in-orbit SLD (slow-LD; subsection 2.3) rate is 1000–1500 $\mathrm{ct\,s^{-1}}$ per well, implying a chance probability of 4–6% for the surrounding 8 units to cause an accidental rejection of a valid GSO signal.

4.6. *Energy Response*

In the same way as the PIN diodes (subsection 3.4), the GEANT4 Monte Carlo toolkit was utilized to construct the GSO energy response function. This technique is particularly important at energies above ~ 100 keV, where the probability of signal photons undergoing Compton scattering increases, and hence off-diagonal elements in the response matrix become significant. Their analytic calculation would be difficult,

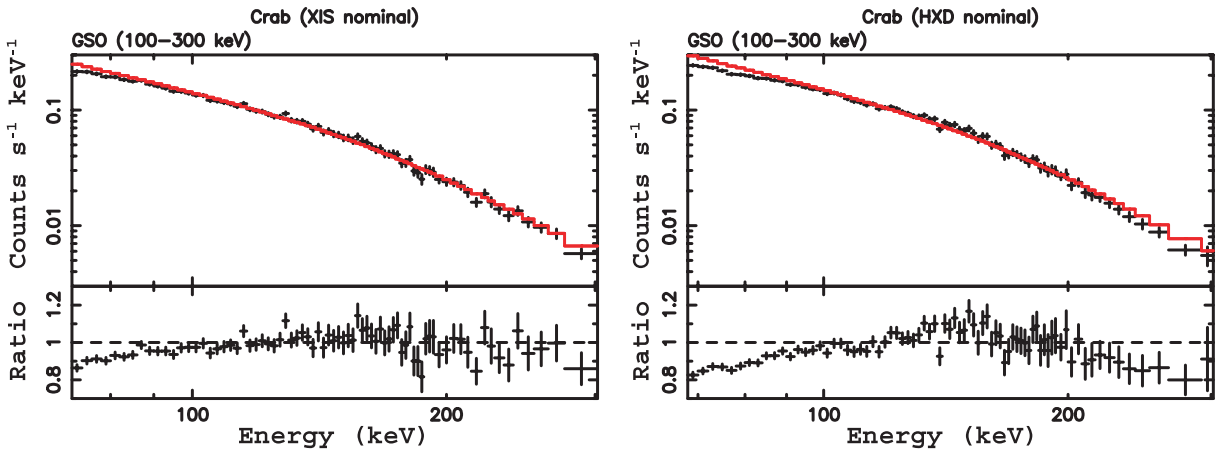

Fig. 18. Background-subtracted Crab spectrum of GSO (summed over the 16 well units), obtained at the XIS nominal (left) and HXD nominal (right) positions, compared with predictions (red) by the best-fit power-law model, of which the parameters are given in table 8. The fittings were carried out in a range of 100–300 keV, and then remaining channels were retrieved. The lower panels show the data-to-model ratio.

Table 8. Best-fit parameters and 90% confidence errors for the GSO spectra of the Crab Nebula at the XIS and HXD nominal positions.*

Target position	Photon index	Normalization†	χ^2_ν (d.o.f)
XIS nominal‡	2.12 ± 0.03	10.6 ± 1.4	1.07 (98)
HXD nominal§	2.15 ± 0.03	11.7 ± 1.4	1.50 (96)

* The column density for the interstellar absorption is fixed at 3×10^{21} cm^{-2}.
† Power-law normalization in units of photons cm^{-2} s^{-1} keV^{-1} at 1 keV.
‡ Observation performed on 2006 April 04 02:55–14:20 (UT)
§ Observation performed on 2006 April 05 12:47–April 06 14:13 (UT).

because it must take into account the probability of a Compton-scattered signal photon to be rejected either by the PSD within the same well unit, or by the anti-coincidence with another unit. The Monte Carlo calculations were performed employing the basic interaction cross sections and detailed detector geometry, as well as light yields of the three scintillator components (GSO, BGO bottom piece, and BGO top piece) measured in pre-launch tests.

Figure 18 shows the GSO spectra (summed over the 16 units) of the Crab Nebula, after subtracting blank-sky background taken on the next day. The backgrounds were extracted using the same "good time interval" conditions as the on-source data, that is, COR $>$ 8, elapsed time from the SAA $>$ 500 s, and elevation from the earth rim $> 5°$. The spectrum was fitted with a single power-law model, using the response function, as constructed above (`ae_hxd_gsoxinom_20060321.rmf` and `ae_hxd_gsohxnom_20060321.rmf`). The fit was performed over the 100–300 keV range so as to avoid a poor signal-to-noise ratio above 300 keV (where the signal becomes $\sim$ 20% of the background) and insufficient tuning of the PSD efficiency and other parameters below 100 keV. Thus, the data were successfully reproduced to within $\pm$10%, and the obtained best-fit parameters, given in table 8, agree within $\sim$ 10% with those determined with PIN (table 6). The remaining task is to improve the fit to the Crab spectrum, and to extend the fit toward lower and higher energies.

5. Non-X-Ray Background

The HXD is designed to achieve a high signal-to-noise ratio by reducing the detector background as much as possible (Paper I). Although the HXD has no capability of rocking on-off observations utilized in the PDS onboard BeppoSAX and the HEXTE onboard RXTE, a high sensitivity can be obtained by subtracting a sufficiently accurate "modeled" non-X-ray background (NXB) instead of the off-observation spectrum. Given the accuracy of in-orbit calibrations, the performance of the experiment solely depends on the reproducibility of the NXB modeling, and hence on the precise knowledge of temporal and spectral NXB variations. In the near-Earth orbit of Suzaku, the HXD field-of-view is blocked periodically by the Earth for a certain fraction of each orbital revolution, and hence the actual in-orbit behavior of the NXB can be constantly monitored using this "Earth occultation" data.

5.1. *Common Properties of the PIN/GSO Background*

Generally, the NXB of a hard X-ray instrument, flown in a low Earth orbit, consists of several components, as follows: a) delayed emissions from radio-active isotopes induced inside the detector, mainly by SAA protons via nuclear interactions, b) prompt secondary radiation caused by interactions between cosmic-ray particles and the spacecraft, and c) intrinsic background caused by natural radioactive isotopes in detector materials. While the third component is constant

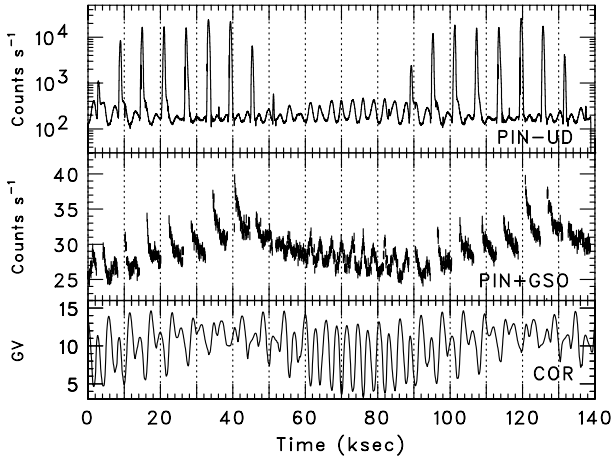

Fig. 19. Typical light curves of the PIN-UD counting rate summed over the 16 units (top), "cleaned" events from PIN and GSO (middle), and the cut-off rigidity (bottom), obtained from ~ 1.5 day observation of a blank sky field.

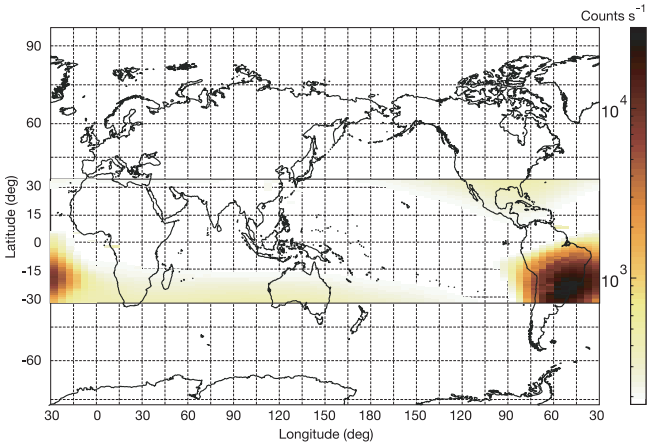

Fig. 20. Flux map of cosmic-rays and trapped particles measured by the PIN-UD count.

throughout the mission, the first and second ones significantly vary in the orbit, corresponding to individual depths of the SAA passages and/or changes in the cosmic-ray fluxes. Therefore, the primary information about the nature of NXB can be obtained by measuring time variations and geographical distributions of such high energy particles. For this purpose, the counting rates of PIN-UD from the 16 well units can be used as a real-time flux monitor, even during the SAA passages (subsection 2.3), by regarding PIN-UD counts per a fixed period as the number of energetic charged particles which penetrated the BGO shields and the passed through the PIN diodes.

Figure 19 shows typical light curves of the total PIN-UD counting rate, the event rate of PIN and GSO after all of the screening procedures have been applied, and the value of COR along the spacecraft orbit. Since these were obtained from a blank-sky observation, the event rate can be roughly regarded as that of the NXB. In the top panel, sharp peaks reaching $\sim 20000\,\mathrm{ct\,s^{-1}}$, which corresponds to a flux of $\sim 100\,\mathrm{ct\,s^{-1}\,cm^{-2}}$, indicate SAA passages. Although this flux is about an order of magnitude lower than the well-known SAA flux at an inclination of 32° (Zombeck 1990), this is because the PIN diodes are embedded in the thick BGO shields, and hence only SAA protons above ~ 100 MeV reach PIN. Outside the SAA, the counting rate is also modulated from ~ 100 to $\sim 400\,\mathrm{ct\,s^{-1}}$ with a period of ~ 3000 s. Its clear anti-correlation with the COR value means that the cut-off energy of cosmic-ray particles decreases when the satellite passes through high-latitudinal regions. The PIN-UD counts integrated for a day are typically $\sim 7\times10^7$, and roughly 90% of them are SAA protons.

The component "a)" mentioned above usually shows complicated variations, since it is a composite of many radioactive isotopes with different half lives. As shown in the middle panel of figure 19, "short-nuclides", which have half-lives shorter than the orbital period (~ 100 min), cause a rapid decrease in the light curve after every SAA passage, while "middle-nuclides", whose decay time constants are longer than the revolution but shorter than a day, produce a gradual increase and a decline over the SAA and non-SAA orbits, respectively. In addition, "long-nuclides", which have lifetimes of a few days to more than a hundred days are gradually accumulated until they individually achieve equilibria between decay and production, and contribute as a constant component in the light curve.

By accumulating the PIN-UD counting rate at a given position of the satellite, and projecting the value onto the corresponding geographical coordinates, a flux map of high-energy particles is obtained, as shown in figure 20. It was confirmed that the SAA has its centroid at around $(320°, -30°)$ with a size of $\sim 60° \times 40°$, at the altitude of Suzaku (~ 570 km). This information is being utilized to generate high-voltage reduction commands in daily operations (subsection 2.2). Since the SAA is known to move westward slowly ($\sim 0.^\circ3$ per year), and the flux of trapped protons is affected by the solar activity, these maps obtained every 50 days were examined for possible temporal changes of the position, size, and intensity of the SAA. Then, the SAA has been confirmed to be quite stable throughout the performance-verification phase.

Even though the properties of the SAA remain unchanged, the daily integrated PIN-UD counts change day by day, mainly due to different total doses caused by different sets of SAA penetration trails of the spacecraft, and to a lesser extent, due to a difference in the satellite attitude as it gets into the SAA. Due to an orbital precession by $\sim 7.^\circ2$ per day, positions of the Suzaku's 15 daily revolutions relative to the SAA change with a period of ~ 50 d. As shown in figure 21, the daily integrated PIN-UD count indeed shows cyclic variations with the same period. The most variable units located at the corner of the 16 well units exhibit a peak-to-peak variation amplitude of $\sim 50\%$, while those of the heavily shielded central four units are smaller than 10%. Although the proton flux in the SAA, itself, varies by a factor of ~ 2 according to the 11-year solar cycle, such a long-term effect is not yet observable within the first year of Suzaku.

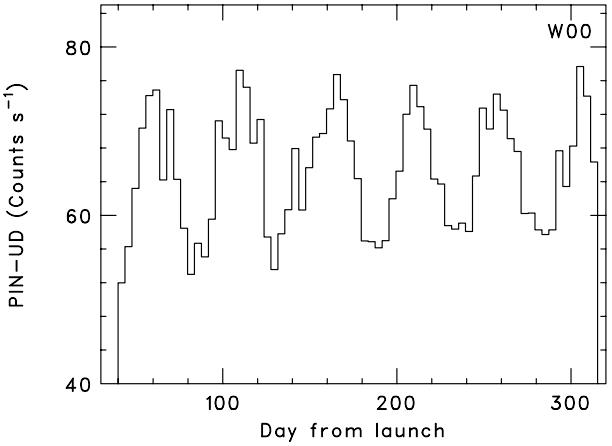

Fig. 21. Light curve of the daily averaged PIN-UD count from a representative well unit.

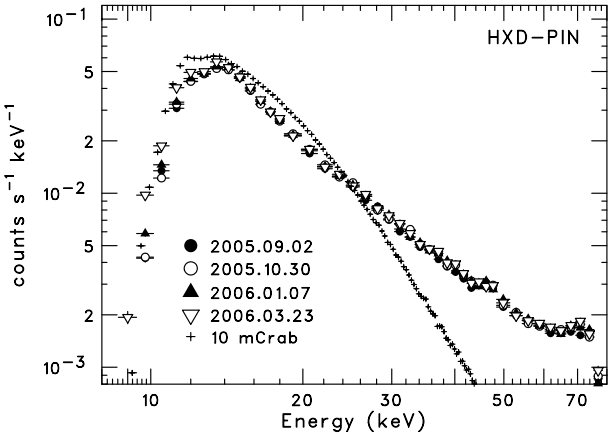

Fig. 22. Comparison of four average NXB spectra measured by HXD-PIN, on 4 occasions separated by two months. Each observation has an exposure longer than two days. The Crab spectrum, scaled down by two orders of magnitude, are also shown.

5.2. *Properties of the Residual Background of PIN*

As sketched in subsection 5.1, the presence of *long-nuclides* would significantly complicate the background reproducibility. This is however not expected to be the case with PIN, since long-lived radioactive isotopes are rare among elements with small atomic numbers, like silicon. Figure 22 compares four NXB spectra of PIN (hereafter PIN-NXB), obtained every two months over half a year. Although blank-sky data contain both cosmic X-ray background (CXB) and NXB, the former is only $\sim 5\%$ of the latter due to the narrow field-of-view ($\sim 34'$) of PIN, and hence the CXB sky fluctuation can be ignored. Above 15 keV, the average PIN-NXB has thus stayed constant within 5%, confirming that the PIN-NXB is free from any long-term accumulation. When compared with a *scaled* Crab spectrum (also shown in figure 22), the average PIN-NXB is roughly equivalent to a 10 mCrab source below 30 keV. This in turn means that a sensitivity of 0.5 mCrab can be achieved by modeling the PIN-NXB spectrum with an accuracy of 5%. Given the absence of *long-nuclides* in the PIN diodes, its background reproducibility is set solely by the accuracy with which the short-term (less than a day) variations can be modeled.

Although the anti-coincidence system of the HXD efficiently works to veto cosmic-ray events in which charged particles interact with the detector, the short-term behavior of NXB is still affected by secondary emissions from interactions between cosmic-ray particles and the spacecraft. In addition, *short-* and *middle-nuclides* induced during SAA passages can also contribute to the NXB variation. The top panel of figure 23 shows a light curve of PIN-NXB folded with an "elapsed time from the SAA (T_SAA)", which is reset to zero at every entry to the SAA. Since only data during the Earth occultations are utilized, the CXB is not included in this case. The bottom panel of figure 23 shows the averaged COR corresponding to each T_SAA, where clear modulation appears because COR and T_SAA are mutually coupled. A strong anti-correlation between the PIN-NXB and COR is evident, whereas the dependence on T_SAA, itself, is rather weak. Therefore, the PIN-NXB is dominated by the cosmic-ray

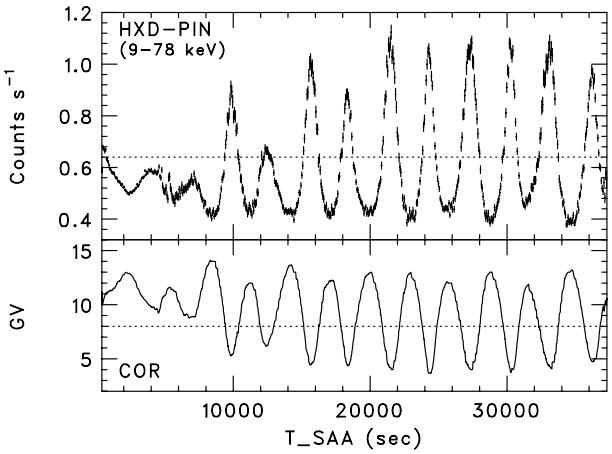

Fig. 23. Light curve of the PIN-NXB folded with T_SAA in the energy range of 9–78 keV (top), and a plot of the cut-off rigidity obtained as an average for each T_SAA (bottom).

component, rather than by the SAA components. The peak-to-peak amplitude of the variation reaches a factor of three, but it is significantly reduced to ~ 1.5 when a selection criterion of COR > 8 is applied, as indicated by the dotted lines in figure 23. With this condition, the average PIN-NXB counting rate is $\sim 0.5\,\mathrm{ct\,s^{-1}}$ over the entire energy range. It in turn means that statistical fluctuations of the integrated PIN-NXB counts become smaller than $\sim 1\%$ when the exposure exceeds 20 ks.

To construct precise models of the PIN-NXB, it is crucial to examine spectral variations as a function of the COR and T_SAA parameters. The left panel of figure 24 shows the PIN-NXB spectra extracted from COR regions of 3–6, 7–10, and 11–15 GV, together with their ratios. When the COR decreases, the PIN-NXB spectrum thus keeps a similar spectral shape below ~ 25 keV, whereas it shows a significant "hardening" above that energy. On the other hand, as shown in the right panel of figure 24, the spectral shape of PIN-NXB depends little on T_SAA, except in the lowermost energies below 12 keV.

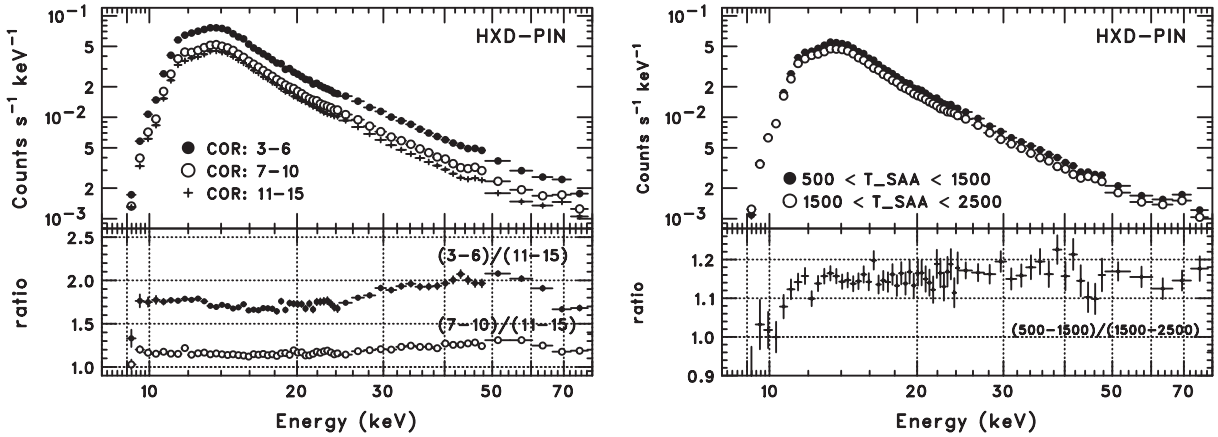

Fig. 24. PIN-NXB spectra sorted with respect to COR (left) and T_SAA (right), extracted from the Earth occultation data. Their ratios are shown in bottom panels.

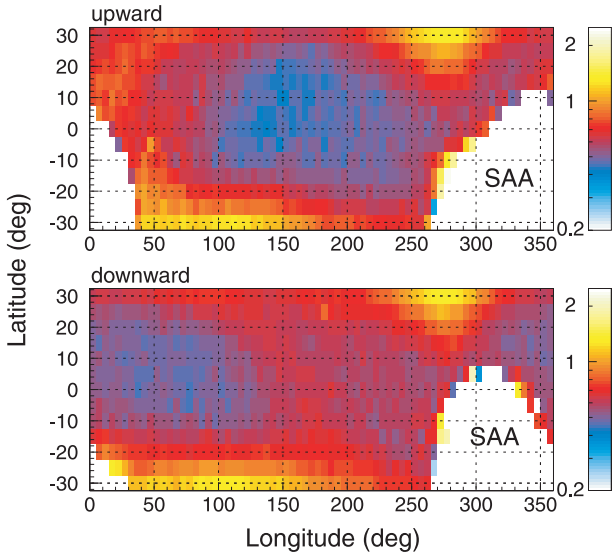

Fig. 25. Maps of the total counting rate of PIN-NXB from the entire energy range, plotted on geographical longitudes and latitudes, when the satellite is moving toward north (top) and south (bottom).

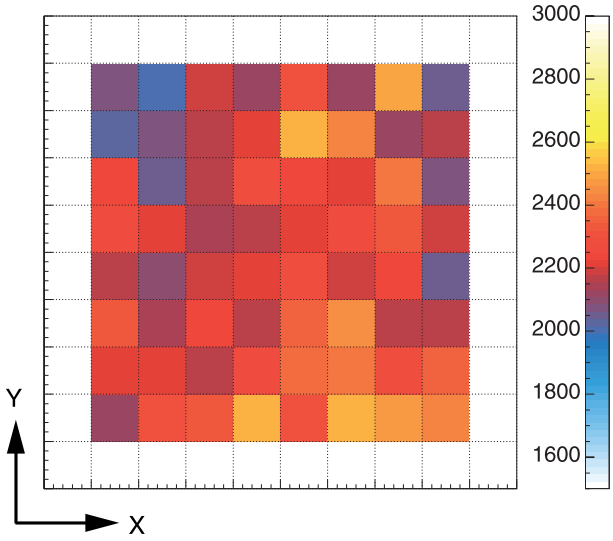

Fig. 26. Distribution of integrated NXB counts from the 64 PIN diodes with a total exposure of $\sim$ 2.3 Ms. The figure is shown as a top view of HXD-S.

The above parameterization of PIN-NXB in terms of COR and T_SAA may be improved by replacing them with geographical longitudes and latitudes, because COR and T_SAA are not actually independent, and because the T_SAA parameter suffers a systematic uncertainty caused by the definition of the SAA boundary. As shown in figure 25, geographical maps of PIN-NXB can be obtained by accumulating the counts as a function of the instantaneous spacecraft position on the Earth. Two different maps are obtained according to the directions of the satellite motion, namely, north-east and south-east. They must be distinguished, because the elapsed time from the SAA at a given position differs between the two directions. The maps reveal two high PIN-NXB regions, roughly coincident with small COR regions at high geomagnetic latitudes. In addition, a slight increase ($\sim$10%) of the PIN-NXB is observed in the top panel just after the SAA passages.

In order to actually construct the NXB model as a function of the geographical position, it is necessary to accumulate Earth occultation data at each position using a sufficiently fine mesh covering the Earth. During the performance verification phase, an average exposure of the Earth occultation was $\sim$ 14 ks per day, and hence the net exposure of $\sim$ 3.3 Ms has already been obtained. This enables an NXB database to be constructed using $\sim$ 160 mesh points, if requiring a minimum exposure of 20 ks each. This correspond to a mesh size of $\sim 30^\circ \times 5^\circ$ on geographical maps. If the 64 PINs have different temporal or spectral variations, the database should be constructed separately for individual PINs, and hence the modeling would become much more difficult. Figure 26 shows distributions of the NXB counts of the individual 64 PIN diodes, obtained in an energy range of 40–55 keV, which is free from the different LD levels. Deviations from the mean are confirmed to remain within $\sim$ 10%, justifying the summed treatment of the 64 PIN diodes.

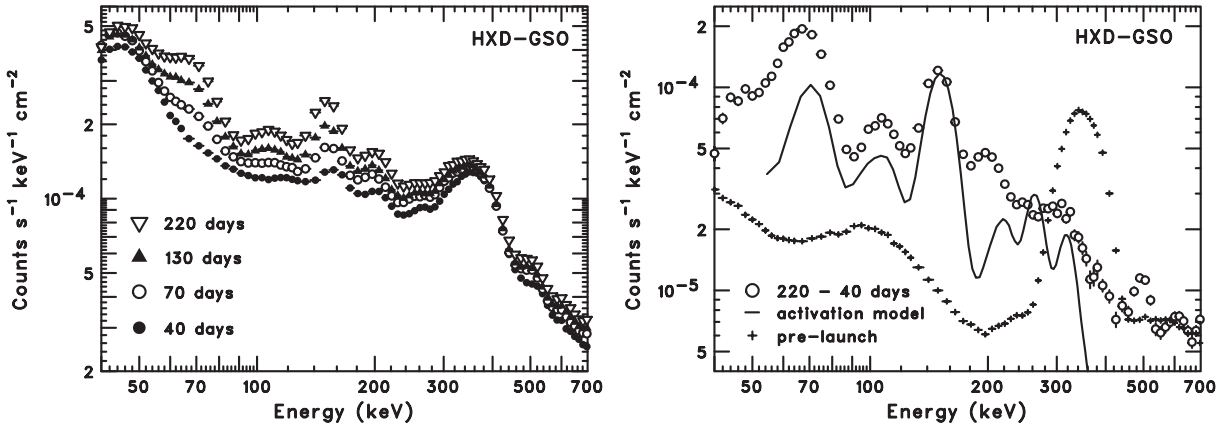

Fig. 27. (Left) Evolution of the averaged GSO-NXB spectra during the first half year after the launch. Each observation has an exposure longer than a day. (Right) A difference GSO-NXB spectrum between 40 and 220 days after the launch (open circles), compared with the estimated long-nuclides spectrum (smooth curve). The pre-launch intrinsic background is also shown (crosses).

5.3. Properties of the Residual Background of GSO

Modeling of the NXB in GSO (hereafter GSO-NXB) is significantly more difficult than that of the PIN-NXB, due to the expected presence of *long-nuclides*. Background levels due to the *long-nuclides*, to be induced in the GSO scintillator by the SAA protons, were estimated before launch, assuming that they have individually achieved equilibria in orbit. The production cross-section for each isotope was calculated based on a semi-empirical formula and ground experiments (Kokubun et al. 1999), and then internal activation spectra of GSO corresponding to decay chains of the individual isotopes were constructed using detailed Monte Carlo simulations. However, the simulations dealt only with nuclides of which the lifetime is longer than a few days, and hence contain neither the short-nuclides nor the secondary emissions from cosmic-ray particles. Therefore, detailed studies of the actual GSO-NXB are of high importance.

Figure 27 shows daily averaged GSO background spectra measured at 40, 70, 130, and 220 days after the launch. The later spectra clearly show several peaks, which are absent or very weak in the 40-day spectrum. These peaks, evolving on a time scale of several months, are due to EC decays of unstable isotopes. In contrast, the continuum up to 400 keV had already reached, in the first 40 days, a relatively constant level at $\sim 1 \times 10^{-4}$ ct s^{-1} keV^{-1} cm^{-2}. Therefore, to cancel the continuum and extract only the "long-nuclides" components, the 40-day spectrum was subtracted from that of 220 days. Figure 27 (right) compares this difference spectrum with the pre-launch estimation. Thus, a good agreement is observed in the positions of the three prominent peaks (70, 100, 150 keV), with a moderate accuracy within a factor of two in their absolute fluxes. The peak at 250 keV in the pre-launch model corresponds to ^{153}Tb, and the over-estimation was probably due to the inadequateness of the semi-empirical formula of the nuclear cross-section employed in the model. The peak at 200 keV directly originates in ^{151m}Eu, an isomer with a significantly short half-life, but its parent nuclei is ^{151}Gd, whose half-life is longer than 100 days (124 d). From this, the three peaks have been identified as shown in table 7 (p.63). The peak at 100 keV is also caused by ^{153}Gd (150 keV peak), but is not listed in table 7, due to its insufficient intensity for the energy-scale calibration.

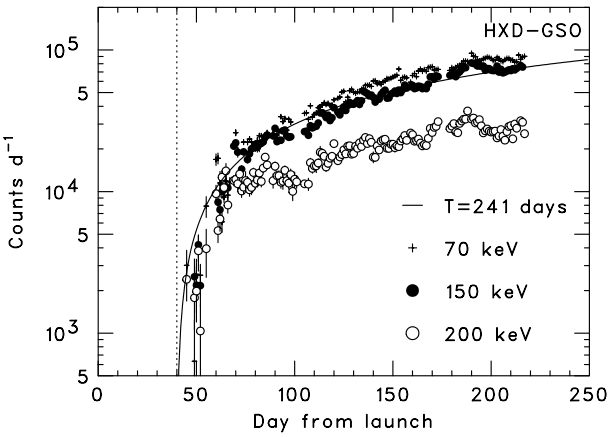

Fig. 28. Light curves of the peak counts of the three prominent EC-decay isotopes, compared with the predicted evolution curve for a half-life of 241 days. The difference spectra were obtained by subtracting the in-orbit background taken at 40 days, as indicated by the dotted line.

Now that individual peaks are thus identified with corresponding isotopes, their in-orbit evolutions can be predicted from their half-lives, assuming that the daily dose during the SAA passages stay constant. Figure 28 compares this prediction with the actually measured long-term evolution of the three prominent peaks, obtained by fitting the difference spectra (with the 40-days spectrum subtracted) with multiple Gaussian functions. The light curve of the 150 keV (^{151}Gd) peak indeed shows a good agreement with a calculation assuming a half-life of 241 days, hence confirming the isotope identification. Since the longest life of the identified isotopes is shorter than one year, the long-term increase in the GSO-NXB is expected to saturate on a time scale of one year. Then, it will show a modulation within a factor of two, anti-correlated with the solar activity cycle.

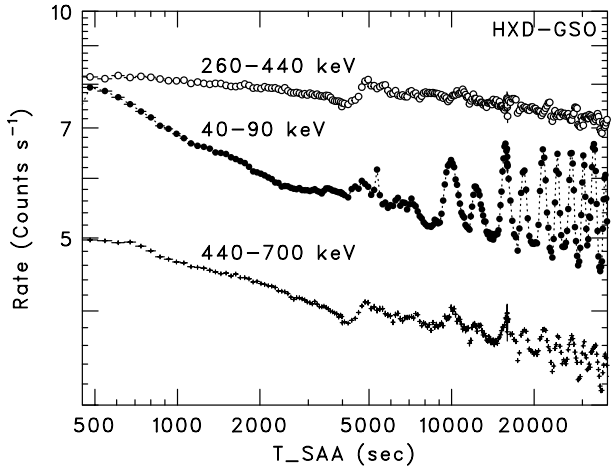

Fig. 29. Light curves of the GSO-NXB in 40–90, 260–440, and 440–700 keV, folded with the T_SAA.

Figure 29 shows the GSO-NXB counts in several broad energy bands, folded with the T_SAA parameter (subsection 5.2). The light curves in the lowest and highest energy bands thus decline rapidly with T_SAA, suggesting the dominance of short-nuclides in the lowest end of the GSO energy range and at around the annihilation line energy. In contrast, the background rate near the intrinsic ^{152}Gd peak (Paper I) is almost independent of T_SAA. In non-SAA orbits that correspond to T_SAA values longer than 5000 s, the GSO-NXB is seen to anti-correlate with COR, in all energy bands but with varying amplitudes, with a maximum of $\sim 40\%$. These results imply that the spectral shape of GSO-NXB depends on both T_SAA and COR.

The GSO-NXB spectra, sorted by COR and T_SAA, are shown in the left and right panels of figure 30, respectively. As expected from figure 29, large variations are found mostly below 150 keV, while the spectral shape stays rather constant at 150–400 keV. The annihilation line, which is probably caused by β^+-decays in the surrounding BGO scintillators or passive materials, becomes obvious when the spectrum during SAA orbits is compared with that during a non-SAA environment, indicating a rapid progress of β^+-decay processes. The ratio spectrum between small and large COR regions shows three prominent peaks, one of which corresponds to the K-edge energy of gadolinium (~ 50 keV). Since prompt emission from the cosmic-ray particle events are already discarded by the hard-wired PSD and mutual anti-coincidence, these peaks suggest the existence of significant short-nuclides induced by the primary events.

5.4. Comparison with Other Missions

As described in subsections 5.1–5.3, the temporal and spectral behavior of the PIN-NXB and GSO-NXB can both be described basically in terms of the satellite position in orbit. Any unexpected or sporadic variations are insignificant, which in turn ensures, at least potentially, an accurate background modeling. Especially, the absence of long-term changes in the PIN-NXB is quite advantageous for constructing an accretion model. In figure 31, the NXB spectra of PIN and GSO, averaged over the performance verification phase, are compared with typical in-orbit detector backgrounds of other non-imaging hard X-ray detectors. In energy ranges of 15–70 and 150–500 keV, the lowest background level has been achieved by the HXD. Since the averaged HXD spectra include both SAA and non-SAA orbits, the HXD backgrounds can be reduced by 2–20%, especially in the GSO background below 100 keV, if data from only non-SAA orbits are employed.

While the sensitivity of rocking detectors are limited by statistical errors in off-source and on-source spectra, that of the HXD is solely determined by the accuracy of background modeling, in the case of background dominant sources. Two types of PIN-NXB models have been developed and tried so far. The first one estimates the background flux at a given time based on the instantaneous PIN-UD rate (summed over the 64 PINs) at that time and the PIN-UD rate time-integrated with a certain decay time constant, while the other employs a model fitting to the PIN-UD light curve from each observation. The results from the two independent methods have been confirmed to agree within an accuracy of 5%, and both have been already applied to scientific analyses of celestial sources

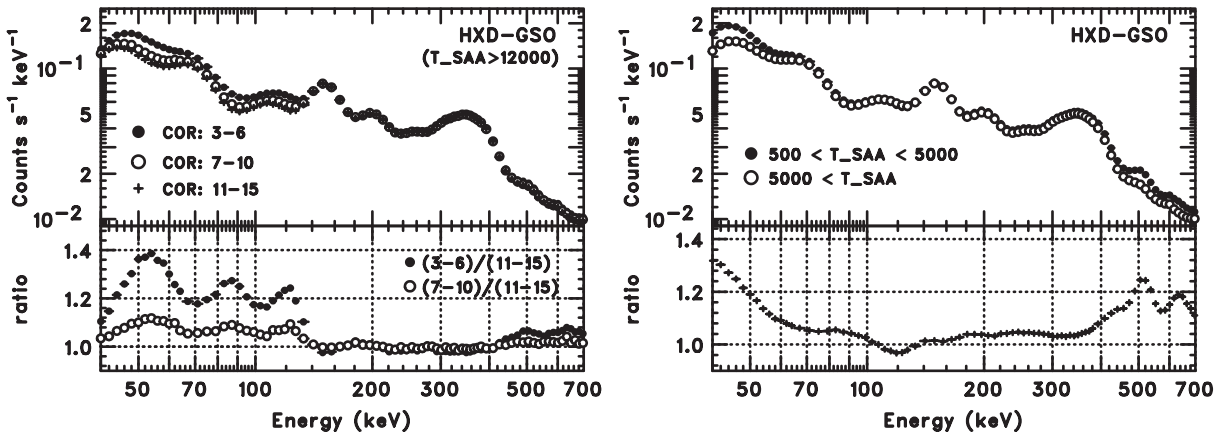

Fig. 30. (Left) GSO background spectra accumulated at several COR regions of non-SAA orbits. (Right) GSO background spectra accumulated from SAA passages (filled circle) and non-SAA orbits (open circle).

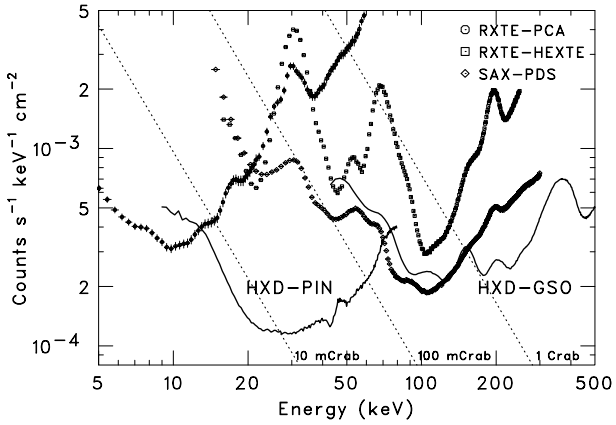

Fig. 31. In-orbit detector background of PIN/GSO, averaged over 2005 August to 2006 March and normalized by individual effective areas. For a comparison, those of the RXTE-PCA, RXTE-HEXTE, and BeppoSAX-PDS are also shown. The dotted lines indicate 1 Crab, 100 mCrab, and 10 mCrab intensities.

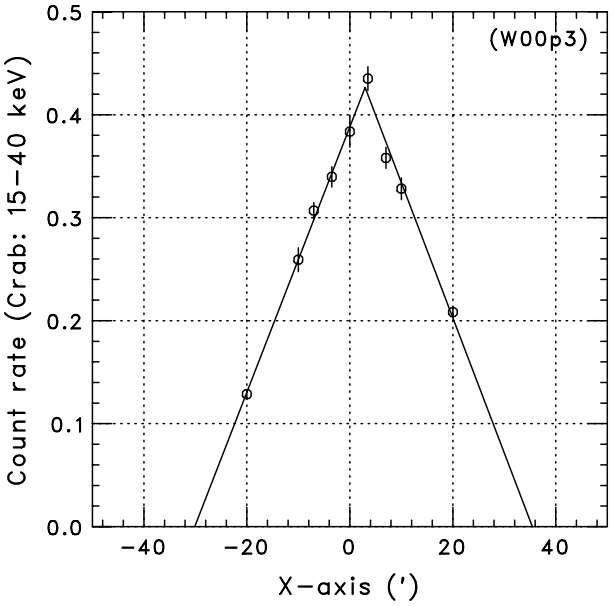

Fig. 32. Typical angular response of a single fine collimator along the satellite X-axis, obtained from nine offset observations of the Crab Nebula.

with an intensity of a few tens of percent of the background. Except the SAA orbits in which the PIN-NXB increases significantly, the reproducibility of both models has been confirmed to be 3–5%. The construction of more accurate models, which are applicable to SAA orbits with an accuracy better than 3%, are in progress; results will be made available to the public.

6. Other Calibration Items

6.1. Angular Response

Individual fields-of-view of the 64 PIN diodes are collimated with 64 passive fine collimators to $\sim 34'$. Although it was confirmed in the on-ground calibrations that the optical axes of all fine collimators are aligned within an accuracy of $3'.5$ (Paper I), in-orbit measurements are inevitable to investigate the launch vibration effect. In addition, the absolute alignment of the HXD optical axis to the spacecraft and the XRT/XIS system must be reconfirmed in orbit. Multiple pointing observations on the Crab Nebula were thus performed, which consisted of $0'$, $3'.5$, $7'$, $10'$, and $20'$ offset positions in both the $\pm X$ and $\pm Y$ directions (Serlemitsos et al. 2007). Background-extracted spectra were constructed for all of the 64 PIN diodes individually, from every observation, and counting rates at that location were obtained in an energy range of 15–40 keV after a dead-time correction (subsection 6.2). These fluxes were plotted against the X- and Y-axes of the spacecraft coordinates, and the X/Y central axis of the collimator was calculated by fitting the flux distribution with a triangular function. An example of X-axis angular response is shown in figure 32. The fitting procedure was repeated, excluding data points closer than $3'.5$ from the center derived from the first trial, since the Crab Nebula is not exactly a point source.

Figure 33 shows the resultant distributions of 64 optical axes of the fine-collimators in the X and Y directions. The alignment of each collimator was determined with a typical error of $\sim 1'$, and the overall scatter among the 64 collimators was confirmed to remain within $3'.5$ (FWHM) from the average.

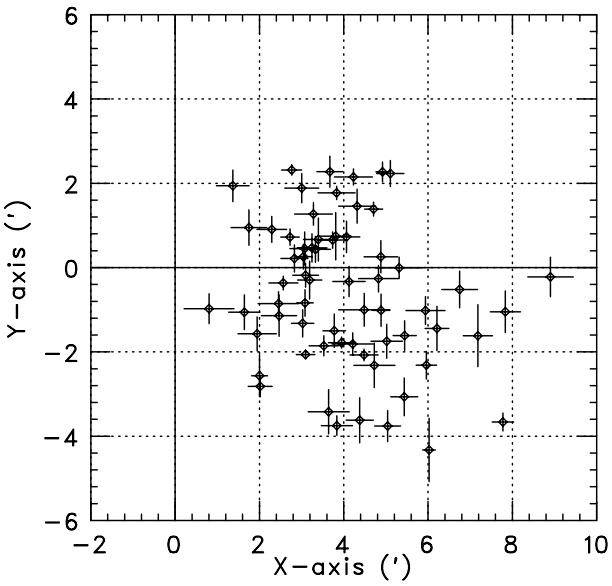

Fig. 33. Summary plot of the distribution of individual optical axes of the 64 fine collimators.

However, the weighted mean shows a slight offset by $\sim 4'$ in the X-direction from the optical axis of Suzaku (i.e., the XIS-nominal position). This offset causes a typical decrease by $\sim 10\%$ in the effective area when an observation is performed at the XIS-nominal position. As shown in figure 34, even at the HXD-nominal position, individual effective areas of the 64 PIN diodes vary at an $\sim 10\%$ level, and hence this effect is taken into account in the energy response matrix.

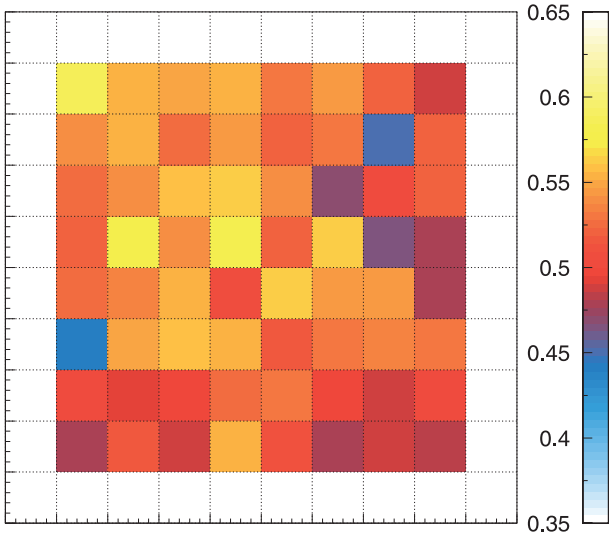

Fig. 34. Distribution of the counting rates of the Crab Nebula, obtained from the 64 PIN diodes in the energy range of 15–40 keV. The observation was performed at the HXD nominal position. The figure illustrates a top view of HXD-S.

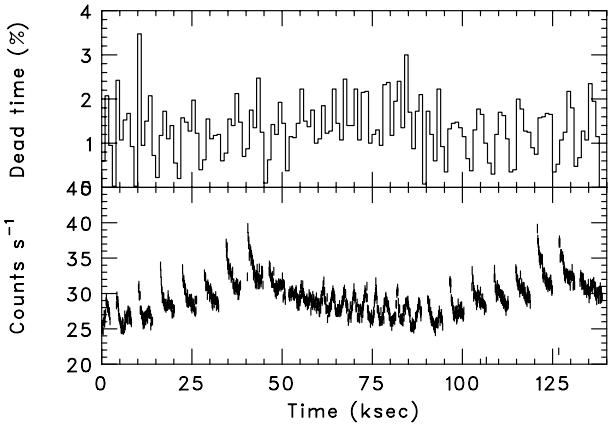

Fig. 35. Typical light curve of the dead-time fraction of HXD (top), and total event rate (bottom), measured during 1.5 days in orbit. Since the event output is disabled during the SAA passages, the actual dead time is 100% in that period.

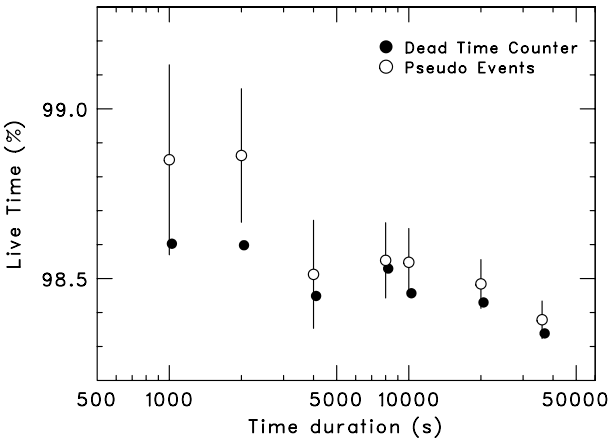

Fig. 36. Comparison of the dead times, calculated with the pseudo-event and the dead-time counter.

6.2. *Dead Time*

The HXD dead time, contained after all of the screening procedures have been applied, is determined by following three factors: the dead time caused by the hard-wired electronics in HXD-AE (Paper I), that due to the limitation of data transfer rate between HXD-AE and HXD-DE, and that due to telemetry saturation. The third case is usually avoided by adequately setting the onboard hardware and software (subsection 2.4), and even if there is any period of the telemetry saturation, that interval will be eliminated by the offline analysis software. To accurately estimate the first and second components, "pseudo-events" are regularly triggered in HXD-AE with a period of an event per four seconds per one well unit (Paper I). Since the pseudo-events are discarded if the pseudo-trigger is generated while a "real event" is inhibiting other triggers, the dead-time fraction can be estimated by counting the number of pseudo-events, output to the telemetry, and comparing with the expected counts during the same exposure. Figure 35 shows a typical light curve of the thus-estimated dead time fraction. Since the event output, except for the pseudo-events, is disabled during the SAA passages, the fraction drops down to nearly zero in every SAA, while it reaches at most $\sim 3\%$ when the event trigger rate becomes high due to activation. These values are consistent with a rough estimation; a multiplication of the average of trigger rate ($\sim 1000\,\mathrm{ct\,s^{-1}}$) and a typical duration of data acquisition sequence ($\sim 25\,\mu\mathrm{s}$).

In addition to the dead time, events can be randomly discarded by both chance coincidence in the hit-pattern flags and PSD selection of GSO. While the latter probability is counted in the energy response matrices of GSO, based on the width of the selection criteria (subsection 4.4), the former can be estimated again using the pseudo-events. Since the hit-pattern signals are latched when the pseudo-trigger has been generated, in the same manner as the real trigger, the chance probability is derived by applying the same anti-coincidence conditions to the pseudo-events as those utilized for the true events, and counting the number of discarded ones. The chance coincidence estimated by this method further reduces an "effective exposure" by 3–5% fraction, which is also consistent with that expected from the width of the hit-pattern signal ($5.6\,\mu\mathrm{s}$) and the averaged counting rate of the SLD ($\sim 1000\,\mathrm{ct\,s^{-1}}$). Since the SLD rate from the well unit is dominated by the activation of BGO scintillators, the chance coincidence probability is hardly affected by the source intensities, which is less than 1% of the average rate, even in case of the Crab Nebula ($\sim 6\,\mathrm{ct\,s^{-1}}$ per well).

The dead-time counter in HXD-AE (Paper I) can be used as another method to estimate the onboard dead time. While the estimation utilizing the pseudo events suffers from a large statistical error in the case of a short exposure, the dead-time counter uses a 156 kHz clock as a base, and hence can accurately estimate even with a short duration. Figure 36 shows a comparison between the two methods at several exposure times. They show an agreement within the statistical error.

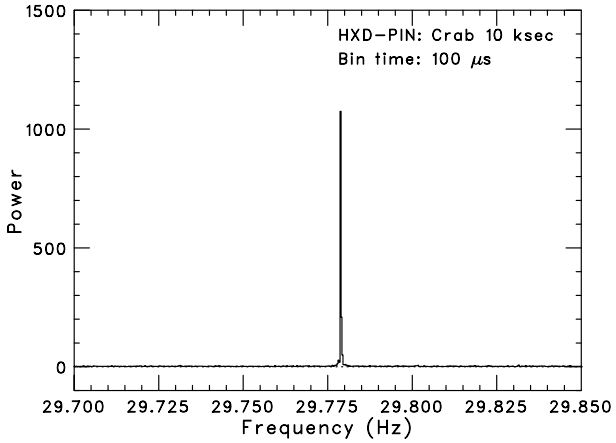

Fig. 37. Power spectrum of the Crab pulsar after the barycentric correction, obtained as the sum of the 64 PIN diodes.

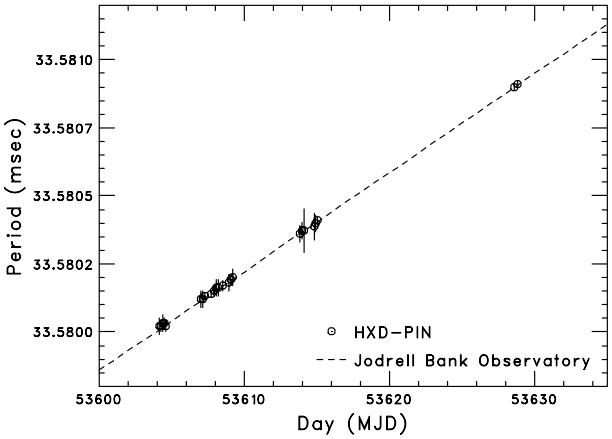

Fig. 38. Pulse periods of the Crab pulsar obtained in the 15–40 keV band with PIN, from 24 observations performed in 2005 August and September. The dashed line shows those measured at the radio wavelength.

6.3. *Timing Accuracy*

The mission requirements on timing are 100 μs to the relative and absolute timing, and a 10^{-8} order of the stability. The arrival time of events detected by the HXD is designed to have a resolution of 61 μs in the "normal" mode, and 31 μs in the "fine" mode. Since only 19 bits per event are reserved for the timing information in the limited word size (16 bytes) of the event data, there is a very large gap in size between the raw data (19 bits) and the mission time records of over 10 years life ($10^{15} \times 100\,\mu$s). The timing system of the HXD is designed to connect with three-types of timing counters: 19 bit event counter with 61 μs to 32 s coverage, timing counter in the central data processing unit (DP) of the satellite with 1/4096 s to 1 Ms, and the ground Cesium clocks at the ground station. All of the timing counters in the Suzaku satellite originate from only one crystal oscillator in DP, which has a timing stability of about 2×10^8 order after correcting any drifts by the variable temperature of the oscillator. The absolute timing is re-calibrated at every time of a contact passage to the ground station, which appears 5 revolutions par day with about 10 minutes duration for each.

In-orbit timing calibrations in the initial phase are performed by X-ray pulsars or binaries, such as the Crab pulsar, PSR 1509−58, and Hercules X-1, with 33 millisecond, 150 millisecond, and $\sim$ 1.0 second period, respectively. As shown in figure 37, clear pulsations were detected from all of the Crab observations, after applying a barycentric correction. The pulse periods derived by the HXD (33.58087 ± 0.00001 ms) show good agreement with that obtained from a simultaneous radio observation (33.5808764 ms). As shown in figure 38, the relative timing stability was thus confirmed to be 10^8 order by a series of simultaneous Crab observations. The pulse profiles obtained at several energy bands, as shown in figure 39, were also confirmed to be consistent with those obtained in a similar band with other gamma-ray missions: RXTE (Rots et al. 2004) and INTEGRAL (Mineo et al. 2006). Besides the hybrid detection devices inside the well unit, the HXD can also detect Gamma-ray bursts (GRBs) by the Anti units with a timing resolution of 15 (or 31) μs (Paper I). The absolute timings

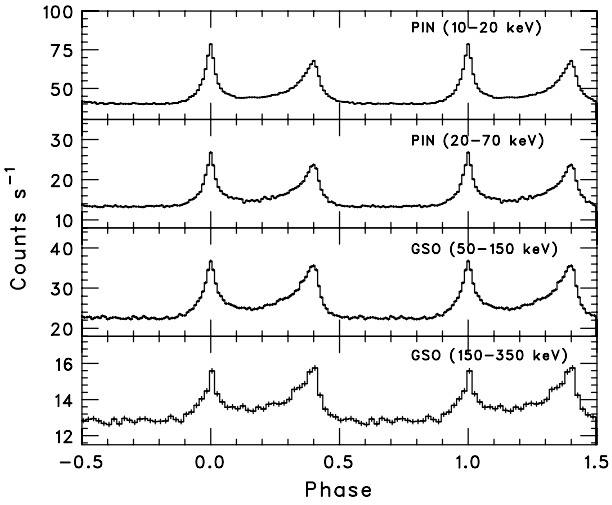

Fig. 39. Folded light curves of the Crab pulsar in four energy bands, obtained as the sum of the 64 PIN diodes or the 16 well units. The observed counts were folded at the pulse period, and are shown for two pulse phases.

are recorded by TPU modules in HXD-AE, and are used for the Inter Planetary Network system. The timing accuracy for GRB triggers was confirmed to be consistent with those by other γ-ray missions, like Swift, Konus-Wind, HETE-2, and INTEGRAL in 2 ms (Yamaoka et al. 2006).

6.4. *Cross-Calibration with XIS*

As described in Koyama et al. (2007) and Serlemitsos et al. (2007), in-orbit calibrations of XISs and XRTs have been extensively performed in parallel with those of the HXD, to realize wide-band spectroscopy with Suzaku. Until now, two instruments have been independently calibrated, and no "adjustment" has yet been performed. Therefore, even though the XIS and HXD always simultaneously observe the Crab Nebula, individual spectral fittings result in slight differences between individual best-fit parameters, on both the

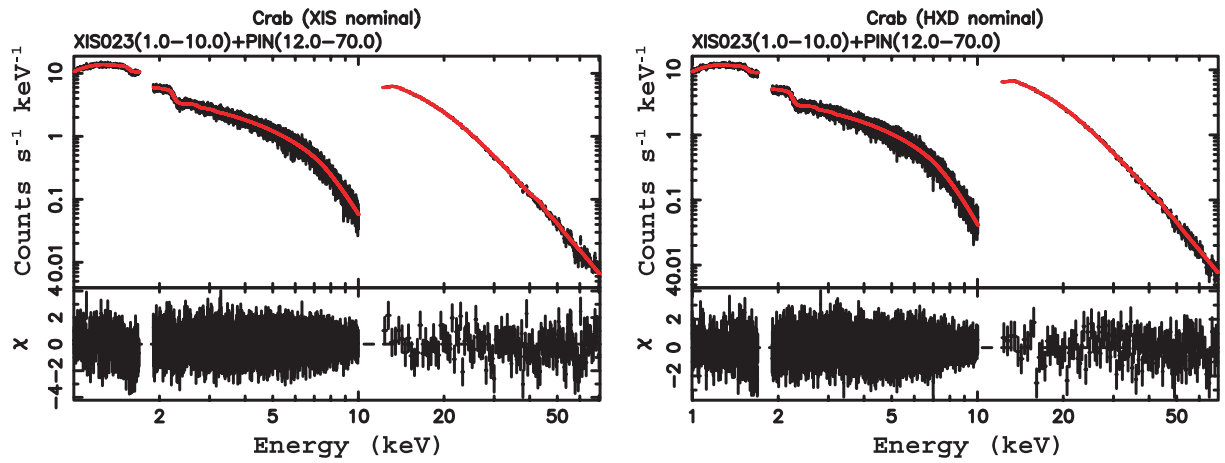

Fig. 40. Background-subtracted Crab spectrum of XIS (summed over the three XIS-FIs) and PIN, compared with the best fit absorbed power-law model. An energy range of 1.7–1.9 keV is excluded from the XIS spectra, due to large systematic uncertainties of the current response matrices (`ae_xi[023]_20060213.rmf` and `ae_xi[023]_[xis/hxd]nom6_20060615.arf`).

Table 9. Best-fit parameters and 90% confidence errors for the spectra of the Crab Nebula at the XIS and HXD nominal positions.

Position	$N_{\rm H}$*	Photon index	Normalization†	Constant factor‡
XIS nominal§	0.32 ± 0.01	2.10 ± 0.01	10.0 ± 0.1	$1.13 \pm 0.01 \pm 0.02$
HXD nominal‖	0.30 ± 0.01	2.09 ± 0.01	9.5 ± 0.1	$1.15 \pm 0.01 \pm 0.02$

* Hydrogen column density in units of $10^{22}\,{\rm cm}^{-2}$.
† Power-law normalization in units of photons $\,{\rm cm}^{-2}\,{\rm s}^{-1}\,{\rm keV}^{-1}$ at 1 keV.
‡ Relative normalization of PIN above XIS.
§ Observation performed on 2005 September 15 19:50–September 16 02:10 (UT)
‖ Observation performed on 2005 September 15 14:00–19:50 (UT).

photon index and the absolute flux at a level of ~ 0.04 and $\sim 15\%$, respectively. As shown in figure 40, the overall spectra can still be reproduced well over a wide energy range of 1–70 keV, when fitted with power-law models having a common photon index and different normalizations between the XIS and PIN. When a "constant factor", which represents the relative normalization of PIN above the average of three front-illuminated CCD cameras (XIS-FIs), is introduced, as shown in table 9, simultaneous fittings with a single power-law model give higher absolute fluxes from PIN diodes than those of the averaged XIS-FIs with a level of $\sim 13\%$ and $\sim 15\%$, at the XIS and HXD nominal positions, respectively. This overestimation infers that thinner depletion layers than true thicknesses were employed in the mass model (subsection 3.4), which remains as an issue to be further investigated.

7. Summary and Conclusion

The results of in-orbit performances and calibrations of the HXD can be summarized by the following points:

1. The initial run-up operations of the HXD and fine tunings of HXD-AE and HXD-DE were completed 40 days after the launch of Suzaku. The instrument was confirmed to have survived the launch vibrations and controlled rapid decrease of temperature with no significant damage.
2. The nominal in-orbit operation mode, which includes the high-voltage levels for PIN diodes and PMTs, fine gain settings, lower and upper threshold levels, and PSD selection conditions for scintillator events were basically established on 2005 August 19, and only slightly changed during the performance-verification phase. The onboard background-reduction system based on the anti-coincidence method was confirmed to function effectively.
3. The in-orbit energy scale of every PIN diode was confirmed to be quite stable, and was accurately determined with an accuracy of 1%. Individual lower energy thresholds ranging 9–14 keV were successfully adopted to the 64 PINs.
4. The in-orbit energy scales of the GSO scintillators were determined in view of the temporal variations. Below 100 keV, they showed additional nonlinearities.
5. The event selection conditions utilized in the analysis software were optimized in terms of the signal acceptance and chance coincidence. The residual in-orbit PIN-NXB level was confirmed to be as low as $\sim 0.5\,{\rm ct\,s}^{-1}$, which corresponds to about 10 mCrab intensity.
6. The temporal and spectral behaviors of the PIN-NXB and GSO-NXB were extensively studied. They show individual dependencies mainly on the cut-off rigidity and elapsed time after the SAA passage, in addition to the long-term accumulation of in-orbit activations.

7. The NXB modeling is still in progress. The current uncertainty of PIN-NXB models are $\sim 5\%$.
8. Energy response matrices of PIN and GSO were constructed, and confirmed to reproduce the Crab spectrum at 12–70 and 100–300 keV energy range, with typical accuracies of $\sim 5\%$ and $\sim 10\%$, respectively.
9. Individual alignments of the 64 fine-collimators were determined in orbit with a typical error of $\sim 1'$.
10. The instrumental dead-time was confirmed to be at the 1–2% level, while the chance coincidence probability further reduces 3–5% of the effective exposure.
11. The HXD timing accuracy was confirmed to be normal.
12. The relative normalization of PIN above the XIS was derived as the 13–15% level, at the current calibration status.

The authors are deeply grateful for dedicated contributions provided by the former members of the development team. This research was partially supported by the Ministry of Education, Culture, Sports, Science and Technology, Grant-in-Aid for Scientific Research for Priority Areas, 14079201, 2006.

References

Agostinelli, S., et al. 2003, Nucl. Instrum. Methods Phys. Res. A, 506, 250
Allison, J., et al. 2006, IEEE Trans. Nucl. Sci., 53, 270
Blackburn, J. K. 1995, in ASP Conf. Ser., 77, Astronomical Data Analysis Software and Systems IV, ed. R. A. Shaw, H. E. Payne, & J. J. E. Hayes (San Francisco: ASP), 367
Frontera, F., Costa, E., dal Fiume, D., Feroci, M., Nicastro, L., Orlandini, M., Palazzi, E., & Zavattini, G. 1997, A&AS, 122, 357
Fukazawa, Y., et al. 2006, Proc. SPIE, 6266, 75
Kawaharada, M., et al. 2004, Proc. SPIE, 5501, 286
Kitaguchi, T., et al. 2006, Proc. SPIE, 6319, 25
Kokubun, M., et al. 1999, IEEE Trans. Nucl. Sci., 46, 371
Koyama, K., et al. 2007, PASJ, 59, S23
Mineo, T., Ferrigno, C., Foschini, L., Segreto, A., Cusumano, G., Malaguti, G., Di Cocco, G., & Labanti, C. 2006, A&A, 450, 617
Mitsuda, K., et al. 2007, PASJ, 59, S1
Ota, N., et al. 1999, Nucl. Instrum. Methods Phys. Res. A, 436, 291
Rothschild, R., et al. 1998, ApJ, 496, 538
Rots, A. H., Jahoda, K., & Lyne, A. G. 2004, ApJ, 605, L129
Serlemitsos, T., et al. 2007, PASJ, 59, S9
Takahashi, T., et al. 2007, PASJ, 59, S35 (Paper I)
Terada, Y., et al. 2005, IEEE Trans. Nucl. Sci., 52, 902
Terada, Y., et al. 2006, ApJ, 648, L139
Uchiyama, Y., et al. 2001, IEEE Trans. Nucl. Sci., 48, 379
Wells, D. C., Greisen, E. W., & Harten, R. H. 1981, A&AS, 44, 363
Yamaoka, K., et al. 2006, Proc. SPIE, 6266, 122
Zombeck, M. V. 1990, Handbook of Space Astronomy and Astrophysics (Cambridge: Cambridge University Press), 233